14

Gas-Kinetic Unified Algorithm for Re-Entering Complex Flows Covering Various Flow Regimes by Solving Boltzmann Model Equation

Zhi-Hui Li[1,2]
[1]*National Laboratory for Computational Fluid Dynamics,*
[2]*Hypervelocity Aerodynamics Institute,*
[2]*China Aerodynamics Research and Development Center,*
China

1. Introduction

Complex flow problems involving atmosphere re-entry have been one of the principal subjects of gas dynamics with the development of spaceflight. To study the aerodynamics of spacecraft re-entering Earth's atmosphere, Tsien (1946) early presented an interesting way in terms of the degree of gas rarefaction, that the gas flows can be approximately divided into four flow regimes based on the order of the Knudsen number (Kn), that is, continuum flow, slip flow, transition flow, and free molecular flow. In fact, the aerothermodynamics around space vehicles is totally different in various flow regimes and takes on the complex characteristics of many scales. In the continuum flow regime with a very small Knudsen number, the molecular mean free path is so small and the mean collision frequency per molecule is so sizeable that the gas flow can be considered as an absolute continuous model. Contrarily in the rarefied gas free-molecule flow regime with a large Knudsen number, the gas molecules are so rare with the lack of intermolecular collisions that the gas flow can but be controlled by the theory of the collisionless or near free molecular flow. Especially, the gas flow in the rarefied transition regime between the continuum regime and free molecular regime is difficult to treat either experimentally or theoretically and it has been a challenge how to effectively solve the complex problems covering various flow regimes. To simulate the gas flows from various regimes, the traditional way is to deal with them with different methods. On the one hand, the methods related to high rarefied flow have been developed, such as the microscopic molecular-based Direct Simulation Monte Carlo (DSMC) method. On the other hand, also the methods adapted to continuum flow have been well developed, such as the solvers of macroscopic fluid dynamics in which the Euler, Navier-Stokes or Burnett-like equations are numerically solved. However, both the methods are totally different in nature, and the computational results are difficult to link up smoothly with various flow regimes. Engineering development of current and intending spaceflight projects is closely concerned with complex gas dynamic problems of low-density flows (Koppenwallner & Legge 1985, Celenligil, Moss & Blanchard 1991, Ivanov & Gimelshein 1998, and Sharipov 2003), especially in the rarefied transition and near-continuum flow regimes.

The Boltzmann equation (Boltzmann 1872 and Chapmann & Cowling 1970) can describe the molecular transport phenomena for the full spectrum of flow regimes and act as the main foundation for the study of complex gas dynamics. However, the difficulties encountered in solving the full Boltzmann equation are mainly associated with the nonlinear multidimensional integral nature of the collision term (Chapmann & Cowling 1970, Cercignani 1984, and Bird 1994), and exact solutions of the Boltzmann equation are almost impractical for the analysis of practical complex flow problems up to this day. Therefore, several methods for approximate solutions of the Boltzmann equation have been proposed to simulate only the simple flow (Tcheremissine 1989, Roger & Schneider 1994, Tan & Varghese 1994, and Aristov 2001). The Boltzmann equation is still very difficult to solve numerically due to binary collisions, in particular, the unknown character of the intermolecular counteractions. Furthermore, this leads to a very high cost with respect to velocity discretization and the computation of the five-dimensional collision integral.

From the kinetic-molecular theory of gases, numerous statistical or relaxation kinetic model equations resembling to the original Boltzmann equation concerning the various order of moments have been put forward. The BGK collision model equation presented by Bhatnagar, Gross & Krook (1954) provides an effective and tractable way to deal with gas flows, which (Bhatnagar et al. 1954, Welander 1954, and Kogan 1958) supposes that the effect of collisions is roughly proportional to the departure of the true velocity distribution function from a Maxwellian equilibrium distribution. Subsequently, several kinds of nonlinear Boltzmann model equations have been developed, such as the ellipsoidal statistical (ES) model by Holway (1963), Cercignani & Tironi (1967), and Andries et al. (2000), the generalization of the BGK model by Shakhov (1968), the polynomial model by Segal and Ferziger (1972), and the hierarchy kinetic model equation similar to the Shakhov model proposed by Abe & Oguchi (1977). Among the main features of these high-order generalizations of the BGK model, the Boltzmann model equations give the correct Prandtl number and possess the essential and average properties of the original and physical realistic equation. Once the distribution function can be directly solved, the macroscopic physical quantities of gas dynamics can be obtained by the moments of the distribution function multiplied by some functions of the molecular velocity over the entire velocity space. Thus, instead of solving the full Boltzmann equation, one solves the nonlinear kinetic model equations and probably finds a more economical and efficient numerical method for complex gas flows over a wide range of Knudsen numbers.

Based on the main idea from the kinetic theory of gases in which the Maxwellian velocity distribution function can be translated into the macroscopic physical variables of the gas flow in normal equilibrium state, some gas-kinetic numerical methods, see Reitz (1981) and Moschetta & Pullin (1997), have been developed to solve inviscid gas dynamics. Since the 1990s, applying the asymptotic expansion of the velocity distribution function to the standard Maxwellian distribution based on the flux conservation at the cell interface, the kinetic BGK-type schemes adapting to compressible continuum flow or near continuum slip flow, see Prendergast & Xu (1993), Macrossan & Oliver (1993), Xu (1998), Kim & Jameson (1998), Xu (2001) and Xu & Li (2004), have been presented on the basis of the BGK model. Recently, the BGK scheme has also been extended to study three-dimensional flow using general unstructured meshes (Xu et al. (2005) and May et al. (2007). On the other hand, the computations of rarefied gas flows using the so-called kinetic models of the original Boltzmann equation have been advanced commendably with the development of powerful computers and numerical methods since the 1960s, see Chu (1965), Shakhov (1984), Yang &

Huang (1995a,b), Aoki, Kanba & Takata (1997) and Titarev & Shakhov (2002). The high resolution explicit or implicit finite difference methods for solving the two-dimensional BGK-Boltzmann model equations have been set forth on the basis of the introduction of the reduced velocity distribution functions and the application of the discrete ordinate technique. In particular, the discrete-velocity model of the BGK equation which satisfies conservation laws and dissipation of entropy has been developed, see Mieussens (2000). The reliability and efficiency of these methods has been demonstrated in applications to one- and two-dimensional rarefied gas dynamical problems with higher Mach numbers in a monatomic gas, see Kolobov et al.(2007).

In this work, we are essentially concerned with developing the gas-kinetic numerical method for the direct solution of the Boltzmann kinetic relaxation model, in which the single velocity distribution function equation can be translated into hyperbolic conservation systems with nonlinear source terms in physical space and time by first developing the discrete velocity ordinate method in the gas kinetic theory. Then the gas-kinetic numerical schemes are constructed by using the time-splitting method for unsteady equation and the finite difference technique in computational fluid dynamics. In the earlier papers, the gas-kinetic numerical method has been successively presented and applied to one-dimensional, two-dimensional and three-dimensional flows covering various flow regimes, see Li & Zhang (2000,2003,2004,2007,2009a,b). By now, the gas-kinetic algorithm has been extended and generalized to investigate the complex hypersonic flow problems covering various flow regimes, particularly in the rarefied transition and near-continuum flow regimes, for possible engineering applications. At the start of the gas-kinetic numerical study in complex hypersonic flows, the fluid medium is taken as the perfect gas. In the next section, the Boltzmann model equation for various flow regimes is presented. Then, the discrete velocity ordinate techniques and numerical quadrature methods are developed and applied to simulate different Mach number flows. In the fourth section, the gas-kinetic numerical algorithm solving the velocity distribution function is presented for one-, two- and three-dimensional flows, respectively. The gas-kinetic boundary condition and numerical methods for the velocity distribution function are studied in the fifth section. Then, the parallel strategy suitable for the gas-kinetic numerical algorithm is investigated to solve three-dimensional complex flows, and then the parallel program software capable of effectively simulating the gas dynamical problems covering the full spectrum of flow regimes will be developed for the unified algorithm. In the seventh section, the efficiency and convergence of the gas-kinetic algorithm will be discussed. After constructing the gas-kinetic numerical algorithm, it is used to study the complex aerodynamic problems and gas transfer phenomena including the one-dimensional shock-tube problems and shock wave inner flows at different Mach numbers, the supersonic flows past circular cylinder, and the gas flows around three-dimensional sphere and spacecraft shape with various Knudsen numbers covering various flow regimes. Finally, some concluding remarks and perspectives are given in the ninth section.

2. Description of the Boltzmann simplified velocity distribution function equation for various flow regimes

The Boltzmann equation (Boltzmann 1872; Chapmann & Cowling 1970; Cercignani 1984) can describe the molecular transport phenomena from full spectrum of flow regimes in the view of micromechanics and act as the basic equation to study the gas dynamical problems.

It represents the relationships between the velocity distribution function which provides a statistical description of a gas at the molecular level and the variables on which it depends. The gas transport properties and the governing equations describing macroscopic gas flows can be obtained from the Boltzmann or its model equations by using the Chapman-Enskog asymptotic expansion method. Based on the investigation to the molecular colliding relaxation from Bhatnagar, Gross and Krook 1954, the BGK collision model equation (Bhatnagar, Gross & Krook 1954; Kogan 1958; Welander 1954) was proposed by replacing the collision integral term of the Boltzmann equation with simple colliding relaxation model.

$$\frac{\partial f}{\partial t} + \vec{V} \cdot \frac{\partial f}{\partial \vec{r}} = -\nu_m (f - f_M) \ , \tag{1}$$

where f is the molecular velocity distribution function which depends on space $\vec{r}$, molecular velocity $\vec{V}$ and time t, f_M is the Maxwellian equilibrium distribution function, and ν_m is the proportion coefficient of the BGK equation, which is also named as the collision frequency.

$$f_M = n/\left(2\pi RT\right)^{3/2} \exp\left[-c^2/(2RT)\right] \ . \tag{2}$$

Here, n and T respectively denote the number density and temperature of gas flow, R is the gas constant, c represents the magnitude of the thermal (peculiar) velocity $\vec{c}$ of the molecule, that is $\vec{c} = \vec{V} - \vec{U}$ and $c^2 = c_x^2 + c_y^2 + c_z^2$. The $\vec{c}$ consists of $c_x = V_x - U$, $c_y = V_y - V$ and $c_z = V_z - W$ along the $x-$, $y-$ and, $z-$ directions, where (U,V,W) corresponds to three components of the mean velocity $\vec{U}$.

The BGK equation is an ideal simplified form of the full Boltzmann equation. According to the BGK approximation, the velocity distribution function relaxes towards the Maxwellian distribution with a time constant of $\tau = 1/\nu_m$. The BGK equation can provide the correct collisionless or free-molecule solution, in which the form of the collision term is immaterial, however, the approximate collision term would lead to an indeterminate error in the transition regime. In the Chapman-Enskog expansion, the BGK model correspond to the Prandtl number, as the ratio of the coefficient of viscosity μ and heat conduction K obtained at the Navier-Stokes level, is equal to unity (Vincenti & Kruger 1965), unlike the Boltzmann equation which agrees with experimental data in making it approximately $2/3$. Nevertheless, the BGK model has the same basic properties as the Boltzmann collision integral. It is considered that the BGK equation can describe the gas flows in equilibrium or near-equilibrium state, see Chapmann & Cowling (1970); Bird (1994); Park (1981) and Cercignani (2000).

The BGK model is the simplest model based on relaxation towards Maxwellian. It has been shown from Park (1981) and Cercignani (2000) that the BGK equation can be improved to better model the flow states far from equilibrium. In order to have a correct value for the Prandtl number, the local Maxwellian f_M in the BGK equation can be replaced by the Eq.(1.9.7) from Cercignani (2000), as leads to the ellipsoidal statistical (ES) model equation (Holway 1966; Cercignani & Tironi 1967 and Andries & Perthame 2000). In this study, the f_M in Eq.(1) is replaced by the local equilibrium distribution function f^N from the

Shakhov model (Shakhov 1968; Morinishi & Oguchi 1984; Yang & Huang 1995 and Shakhov 1984). The function f^N is taken as the asymptotic expansion in Hermite polynomials with local Maxwellian f_M as the weighting function.

$$f^N = f_M \cdot \left[1 + (1-\mathrm{Pr})\vec{c}\cdot\vec{q}\left(c^2/(RT) - 5\right)/(5PRT)\right] \quad . \tag{3}$$

Here, Pr is the Prandtl number with $\mathrm{Pr} = \mu C_p / K$ and is equal to $2/3$ for a monatomic gas, C_p is the specific heat at constant pressure, and $\vec{q}$ and P respectively denote the heat flux vector and gas pressure. It can be shown that if $\mathrm{Pr} = 1$ is set in Eq.(3), the BGK model is just recovered with $f^N = f_M$.

According to the relaxation time approximation (Chapmann & Cowling 1970), the collision frequency ν_m in Eq.(1) can be extended and related to the kinetic temperature as a measure of the variance of all thermal velocities in conditions far from equilibrium by using the temperature dependence of the coefficient of viscosity. The nominal collision frequency (inverse relaxation time) can be taken in the form

$$\nu = nkT/\mu \quad , \tag{4}$$

where n is the number density, k is Boltzmann's constant, and $\mu = \mu(T)$ is the coefficient of the viscosity. Since the macroscopic flow parameters at any time at each point of the physical space are derived from moments of f over the velocity space in the kinetic theory of gases, the collision frequency ν is variable along with the space $\vec{r}$, time t, and thermal velocity $\vec{c} = \vec{V} - \vec{U}$. Consequently, this collision frequency relationship can be extended and applied to regions of extreme non-equilibrium, see Bird (1994); Park (1981) and Cercignani (2000).

The power law temperature dependence of the coefficient of viscosity can be obtained (Bird 1994 and Vincenti & Kruger 1965) from the Chapman-Enskog theory, which is appropriate for the inverse power law intermolecular force model and the VHS (Variable Hard Sphere) molecular model.

$$\mu/\mu_\infty = (T/T_\infty)^\chi \quad , \tag{5}$$

where χ is the temperature exponent of the coefficient of viscosity, that can also be denoted as $\chi = (\zeta+3)/(2(\zeta-1))$ for the Chapman-Enskog gas of inverse power law, ζ is the inverse power coefficient related to the power force F and the distance r between centers of molecules, that is $F = \kappa / r^\zeta$ with a constant κ.

The viscosity coefficient μ_∞ in the free stream equilibrium can be expressed in terms of the nominal freestream mean free path λ_∞ for a simple hard sphere gas.

$$\mu_\infty = \frac{5}{16} m n_\infty (2\pi R T_\infty)^{1/2} \lambda_\infty \quad . \tag{6}$$

Here, the subscripts ∞ represent the freestream value.

The collision frequency ν of the gas molecules can be expressed as the function of density, temperature, the freestream mean free path, and the exponent of molecular power law by the combination of Eqs.(4), (5), and (6).

$$\nu = \frac{16}{5} \cdot \sqrt{\frac{R}{2\pi}} \cdot \frac{T_\infty^{\chi-1/2}}{n_\infty} \cdot \frac{n}{T^{\chi-1}} \cdot \frac{1}{\lambda_\infty} \ . \tag{7}$$

It is, therefore, enlightened that the Boltzmann collision integral can be replaced by a simplified collision operator which retains the essential and non-equilibrium kinetic properties of the actual collision operator. Then, however, any replacement of the collision function must satisfy the conservation of mass, momentum and energy expressed by the Boltzmann equation. We consider a class of Boltzmann model equations of the form

$$\frac{\partial f}{\partial t} + \vec{V} \cdot \frac{\partial f}{\partial \vec{r}} = \nu (f^N - f) \ . \tag{8}$$

Where the collision frequency ν in Eq.(7) and the local equilibrium distribution function f^N in Eq.(3) can be integrated with the macroscopic flow parameters, the molecular viscosity transport coefficient, the thermodynamic effect, the molecular power law models, and the flow state controlling parameter from various flow regimes, see Li & Zhang (2004) and Li (2003).

Actually for non-homogeneous gas flow, the interaction of gas viscosity is produced from the transfer of molecular momentum between two contiguous layers of the mass flow due to the motion of molecules. However, when the gas mass interchanges between the two layers with different temperature, the transfer of heat energy results in the thermodynamic effect. The thermodynamic effect of the real gas flow is reflected in the Eq.(3) of the f^N by using the Prandtl number to relate the coefficient of viscosity with heat conduction from the molecular transport of gas. All of the macroscopic flow variables of gas dynamics in consideration, such as the density of the gas ρ, the flow velocity $\vec{U}$, the temperature T, the pressure P, the viscous stress tensor τ and the heat flux vector $\vec{q}$, can be evaluated by the following moments of the velocity distribution function over the velocity space.

$$n(\vec{r},t) = \int f(\vec{r},\vec{V},t) d\vec{V} \ , \ \rho(\vec{r},t) = mn(\vec{r},t) \ , \tag{9}$$

$$n\vec{U}(\vec{r},t) = \int \vec{V} f(\vec{r},\vec{V},t) d\vec{V} \ , \tag{10}$$

$$\frac{3}{2} nRT(\vec{r},t) = \int \frac{1}{2} c^2 f(\vec{r},\vec{V},t) d\vec{V} \ , \tag{11}$$

$$P(\vec{r},t) = n(\vec{r},t) kT(\vec{r},t) \ , \tag{12}$$

$$\tau_{ij}(\vec{r},t) = m \int c_i c_j f(\vec{r},\vec{V},t) d\vec{V} - P\delta_{ij} \ , \tag{13}$$

$$\vec{q}(\vec{r},t) = m \int \frac{1}{2} c^2 \vec{c} f(\vec{r},\vec{V},t) d\vec{V} \ . \tag{14}$$

Where m denotes the molecular mass, R is the gas constant, k is the Boltzmann's constant, and the subscripts i and j each range from 1 to 3, where the values 1, 2, and 3 may be identified with components along the $x-$, $y-$, and $z-$ directions, respectively.

Since the formulated problem involves in the scale of the microscopic statistical distribution and the macroscale of gas flow with tremendous difference of dimension order, the nondimensionalized procedure of variables and equations is needed to unify the scale in practical computation. Generally, four independent reference variables should be set in the non-dimensional reference system of the computation of gas flows. In here, let L_{ref}, T_∞, n_∞, and m be, respectively, the reference length, the free-stream temperature, the free-stream number density, and molecular mass, put the reference speed and time as $c_{m\infty}=\sqrt{2RT_\infty}$ and $t_\infty = L_{ref}/c_{m\infty}$. Then, the non-dimensional variables are defined as time $\tilde{t}=t/t_\infty$, flow velocity $\tilde{U}_i = U_i/c_{m\infty}$, molecular velocity $\tilde{V}_i = V_i/c_{m\infty}$, $(i=1,2,3)$, number density of gas flow $\tilde{n}=n/n_\infty$, temperature $\tilde{T}=T/T_\infty$, pressure $\tilde{p}=p/(mn_\infty c_{m\infty}^2/2)$, stress tensor $\tilde{\tau}_{ij}=\tau_{ij}/(mn_\infty c_{m\infty}^2/2)$, heat flux vector $\tilde{q}_i = q_i/(mn_\infty c_{m\infty}^3/2)$, space position $\tilde{x}=x/L_{ref}$, $\tilde{y}=y/L_{ref}$, $\tilde{z}=z/L_{ref}$, collision frequency $\tilde{\nu}=\nu\cdot t_\infty$, velocity distribution function $\tilde{f}=f/(n_\infty/(c_{m\infty}^3))$, Maxwellian distribution $\tilde{f}_M = f_M/(n_\infty/c_{m\infty}^3)$, local equilibrium distribution $\tilde{f}^N = f^N/(n_\infty/(c_{m\infty}^3))$. The dimensionless velocity distribution function equation can be obtained with the above non-dimensional variables,

$$\frac{\partial \tilde{f}}{\partial \tilde{t}} + \tilde{\vec{V}}\cdot\frac{\partial \tilde{f}}{\partial \tilde{\vec{r}}} = \tilde{\nu}(\tilde{f}^N - \tilde{f}), \tag{15}$$

$$\tilde{f}^N = \tilde{f}_M\cdot[1+(1-\mathrm{Pr})\tilde{\vec{c}}\cdot\tilde{\vec{q}}(2\tilde{c}^2/\tilde{T}-5)/(5\tilde{P}\tilde{T}/2)], \tag{16}$$

$$\tilde{f}_M = \frac{\tilde{n}}{(\pi\tilde{T})^{3/2}}\exp(-\tilde{c}^2/\tilde{T}), \tag{17}$$

$$\tilde{\nu} = \frac{8\tilde{n}\tilde{T}^{1-\chi}}{5\sqrt{\pi}Kn} \quad , \quad Kn = \frac{\lambda_\infty}{L_{ref}}. \tag{18}$$

Where Kn is the Knudsen number as an important parameter characterizing the degree of rarefaction of the gas, λ_∞ is the free-stream mean free path, and $\tilde{\vec{c}}$ represents the thermal velocity of the molecule, that is $\tilde{\vec{c}} = \tilde{\vec{V}} - \tilde{\vec{U}}$.

Similarly, the non-dimensional macroscopic variables can be represented by non-dimensionalizing Eqs. (9)~(14). In the following computation, all of the variables will have been nondimensionalized, and the "~" sign in the equations will be dropped for the simplicity and concision without causing any confusion.

The equation (15) provides the statistical description of the gas flow in any non-equilibrium state from the level of the kinetic theory of gases. Since mass, momentum and energy are conserved during molecular collisions, the equation (15) satisfies the Boltzmann's H-theorem and conservation conditions at each of points in physical space and time,

$$\int (f^N - f)\psi^{(m)} d\vec{V} = 0. \tag{19}$$

Where $\psi^{(m)}$ are the components of the moments on mass, momentum and energy, that is

$$\psi^{(1)} = 1,\ \psi^{(2)} = \vec{V},\ \psi^{(3)} = \left|\vec{V}\right|^2/2. \tag{20}$$

3. Development and application of the discrete velocity ordinate method in gas kinetic theory

3.1 Discrete velocity ordinate method

The focus under consideration is how the velocity distribution function can be numerically solved. The distribution function f is a probability density function of statistical distribution (Riedi 1976, Chapmann & Cowling 1970, and Park 1981) with seven independent variables (for three-dimensional cases). In order to replace the continuous dependency of f on the velocity space, the discrete ordinate technique, see Huang & Giddens (1967), can be introduced and developed from the point of view of gas kinetic theory. The discrete ordinate method (Huang & Giddens 1967) is based on the representation of functions by a set of discrete points that coincide with the evaluation points in a quadrature rule, which consists of replacing the original functional dependency on the integral variable by a set of functions with N elements $W_i p(x_i)$ ($i = 1, \cdots, N$), where the points x_i are quadrature points and W_i are the corresponding weights of the integration rule.

$$\int_a^b W(x)p(x)dx = \sum_{i=1}^{N} W_i p(x_i) \quad . \tag{21}$$

The interval $[a,b]$ will be either $[0,\infty]$ or $[-\infty,\infty]$ for the application considered and a different weight function $W(x)$ is chosen for each problem considered. The x_i are the roots of the Nth order polynomial $R_n(x)$ of the set that satisfy,

$$\int_a^b W(x)R_n(x)R_i(x)dx = \delta_{in} \quad , \tag{22}$$

where the set of polynomials $R_n(x)$, orthonormal with respect to the weight function $W(x)$ on the interval $[a,b]$, form a complete basis of the $L^2[a,b]$ Hilbert space. The first N of these polynomials form a subspace of this Hilbert space which is isomorphic with the $\Re^N$ Euclidean space. It may be shown from the treatment of the integral over the interval $[a,b]$ with the quadrature rule Eq.(21) that the discrete ordinate representation is equivalent to the truncated polynomial representation of the Nth order.

It's shown from Brittin (1967) and Riedi (1976) that, in general, the velocity distribution function f for states removed from equilibrium is proportional to $\exp(-c^2)$ just as it is for equilibrium, that f has finite bounds under the specific precision in velocity space and tends to zero as c tends to infinity. That is, the integration of the normalized distribution function over all the velocity space should yield unity, and the probability of the molecular velocities far removed from the mean velocity $\vec{U}$ of the flow is always negligible. Thus, in order to replace the continuous dependency of the molecular velocity distribution function on the velocity space, the discrete ordinate technique can be introduced in the kinetic theory of gases to discretize the finite velocity region removed from $\vec{U}$. The choice of the discrete velocity ordinate points in the vicinity of $\vec{U}$ is based only on the moments of the distribution functions over the velocity space. Consequently the numerical integration of the macroscopic flow moments in Eq.(9)–(14) of the distribution function f over velocity space can be adequately performed by the same quadrature rule, with f evaluated at only a few

discrete velocity points in the vicinity of $\vec{U}$. The selections of the discrete velocity points and the range of the velocity space in the discrete velocity ordinate method are somewhat determined by the problem dependent.

Applying the discrete velocity ordinate method to Eq.(15) for the (V_x, V_y, V_z) velocity space, see Li (2003) and Li & Zhang (2009a), the single velocity distribution function equation can be transformed into hyperbolic conservation equations with nonlinear source terms at each of discrete velocity grid points.

$$\frac{\partial Q}{\partial t}+\frac{\partial F^x}{\partial x}+\frac{\partial F^y}{\partial y}+\frac{\partial F^z}{\partial z}=\overline{S} \tag{23}$$

with

$$Q=f_{\sigma,\delta,\theta}\ ,\ F^x=V_{x\sigma}Q\ ,\ F^y=V_{y\delta}Q\ ,$$

$$F^z=V_{z\theta}Q\ ,\ \overline{S}=\nu\left(f^N_{\sigma,\delta,\theta}-f_{\sigma,\delta,\theta}\right)\ ,$$

where $f_{\sigma,\delta,\theta}$ and $f^N_{\sigma,\delta,\theta}$ respectively denote values of f and f^N at the discrete velocity ordinate points $(V_{x\sigma}, V_{y\delta}, V_{z\theta})$, the subscripts σ, δ and θ represent the discrete velocity grid indexes in the V_x-, V_y- and V_z- directions, respectively.

3.2 Development of numerical integration methods for evaluating macroscopic flow moments

Once the discrete velocity distribution functions $f_{\sigma,\delta,\theta}$ are solved, the macroscopic flow moments at any time in each point of the physical space can be obtained by the appropriate discrete velocity quadrature method. In terms of the symmetric quality of the exponential function $\exp(-V^2)$ over the interval $[-\infty,\infty]$, the Gauss-Hermite half-range quadrature can be extended to evaluate of the infinite integral over all the velocity space of the velocity distribution function. The discrete velocity points and the weights corresponding to the Gauss-Hermite quadrature can be obtained using the algorithms described by Huang and Giddens (1967) and by Shizgal (1981), which can be used to approximate the integrals with the exponential type as follows:

$$\int_0^\infty e^{-V^2}p(V)dV\approx\sum_{\sigma=1}^{N}W_\sigma p(V_\sigma) \tag{24}$$

where V_σ $(\sigma=1,\cdots,N)$ are the positive roots of the Hermite polynomial of degree N, W_σ are the corresponding weights, the subscript σ is the discrete velocity index, and $p(V)$ denotes the function which can be derived from the integrands in Eq.(9)–(14). According to Kopal's discussion (Kopal 1955), it is known that for a given number of discrete subdivisions of the interval $(0,+\infty)$, the Gauss-Hermite's choice of the discrete velocity points V_σ and the corresponding weights W_σ yields the optimal discrete approximation to the considered integration in the sense. The Gauss-Hermite's V_σ and W_σ can be tabulated in the table of

the Gauss-Hermite quadrature. However, the number of the discrete velocity points is limited in this way, as it's very difficult exactly to solve high-order Hermite polynomial. The V_σ and W_σ can also be obtained by directly solving the nonlinear Eqs.(24) and (25) in terms of the decomposing principle.

$$\int_0^\infty e^{-u^2} u^k du = \frac{1}{2}\Gamma(\frac{k+1}{2}) \tag{25}$$

It is shown from the computing practice (Li 2001) that it is difficult to ensure the numerical stability with the computation of Eq.(24) and Eq.(25) when the number of discrete velocity points is greatly increased, this indicates that farther application of the Gauss-Hermite quadrature method to high speed gas flows may be restricted. To resolve this deficiency, the specific Gauss-type integration methods, such as the Gauss quadrature formulas with the weight function $2/\pi^{1/2}\exp(-V^2)$ and the Gauss-Legendre numerical quadrature rule whose integral nodes are determined by using the roots of the kth-order Legendre polynomials, have been presented and applied to simulate hypersonic flows with a wide range of Mach numbers.

The basic idea of the Gauss-type quadrature method (Henrici 1958) is to choose the fixed evaluation points V_σ and the corresponding weight coefficients W_σ of the integration rule in a way that the following approximation is exact.

$$\int_D W(V) f(V) dV \approx \sum_{\sigma=1}^{N} W_\sigma f(V_\sigma) \tag{26}$$

If both limits of the integration are infinite, a weighting function must be chosen that goes to zero for both positive and negative values of V. To develop the Gaussian integration method for the supersonic flows, the bell-shaped Gauss-type distribution function is introduced

$$W(V) = \frac{2}{\pi^{1/2}}\exp(-V^2), \quad -\infty < V < \infty. \tag{27}$$

When this weighting function (27) is used over the interval $[0,\infty)$, according to Eq.(26), the resulting Gauss quadrature formula with the weight function $2/\pi^{1/2}\exp(-V^2)$ is referred to as

$$\int_0^\infty \frac{2}{\pi^{1/2}}\exp(-V^2) f(V) dV \approx \sum_{\sigma=1}^{N} W_\sigma f(V_\sigma). \tag{28}$$

Where V_σ $(\sigma = 1,\cdots,N)$ are the positive roots of the orthogonal polynomials, $p_\sigma(V)$, in which the polynomials are generated by the following recurrence relation.

$$p_\sigma(V) = (V - b_\sigma) p_{\sigma-1}(V) - g_\sigma p_{\sigma-2}(V) \tag{29}$$

with $p_0(V) = 1$ and $p_{-1}(V) = 0$. Here, b_σ and g_σ are the recurrence relation parameters (Golub & Welsch 1981) for the orthogonal polynomials associated with $\exp(-V^2)$ on $[0,\infty)$.

The nodes V_σ and weights W_σ of the Gauss quadrature rule (28) can be calculated from the recurrence relation by applying the QR algorithm (Kopal 1955) to determine the eigenvalues

and the first component of the orthonormal eigenvectors of the associated $N \times N$ tridiagonal matrix eigensystem. The Gaussian quadrature will exactly integrate a polynomial of a given degree with the least number of quadrature points and weights. In particular, M -point Gaussian quadrature exactly integrates a polynomial of degree $2M-1$. Therefore, the use of the Gaussian quadrature points and weights would seem to be the optimum choice to the considered integration in the sense, see Li & Zhang (2009a,b).

Since the discrete velocity solution can be treated in terms of expansion on the basis of piecewise constant functions, the computation of the moments of the distribution function can be performed by the network in the discretized velocity space. For example, the gas density is evaluated by the Gauss quadrature formula with the weight function $2/\pi^{1/2}\exp(-V^2)$ in the following manner.

$$n=\int_{-\infty}^{\infty}\int_{-\infty}^{\infty}\int_{-\infty}^{\infty} f dV_x dV_y dV_z \approx \frac{\pi^{3/2}}{8}\sum_{\theta=-N_3}^{N_3}\sum_{\delta=-N_2}^{N_2}\sum_{\sigma=-N_1}^{N_1} W_\theta W_\delta W_\sigma f_{\sigma,\delta,\theta} e^{V_{x\sigma}^2} e^{V_{y\delta}^2} e^{V_{z\theta}^2} . \tag{30}$$

The other macroscopic flow moments, such as mean velocity, temperature, stress tensor and heat flux vector components, can be similarly evaluated according to the Gauss-type quadrature formula (28).

As the aforementioned Gauss-type quadrature rule with the weight function $2/\pi^{1/2}\exp(-V^2)$ merely employs some finite evaluation points to integrate the flow moments over the whole of velocity space, in practical application, it is quite efficacious to evaluate the macroscopic flow variables with high precision, in particular for intermediate Mach number flows. However, for hypersonic flows with high Mach numbers, the velocity distribution severely deviates from the Maxwellian equilibrium with a long trail of the unsymmetrical bimodal distribution in the real line of the velocity space, so that the extensive region of the velocity space depended on distribution function needs to be discretized in quite a wide range, the number of discrete velocity ordinate points needed to cover the appropriate velocity range becomes quite large, and then the composite Gauss-Legendre quadrature rule is developed and applied to this study. The Gauss-Legendre quadrature formula for evaluation of definite integrals with the interval $[-1,1]$ can be written as

$$\int_{-1}^{1} f(t)dt \approx \sum_{i=1}^{n} A_i f(t_i) , \tag{31}$$

where t_i is the evaluation point taken as the roots of a special family of polynomials called the Legendre polynomials, in which the first two Legendre polynomials are $p_0(t)=1$ and $p_1(t)=t$, and the remaining members of the sequence are generated by the following recurrence relation.

$$(n+1)p_{n+1}(t)=(2n+1)tp_n(t)-np_{n-1}(t) , \ n\geq 1 . \tag{32}$$

The corresponding weight coefficients A_i in Eq.(31) are defined by the differential equation with the form

$$A_i=\frac{2}{(1-t_i^2)[p_n^{'}(t_i)]^2} . \tag{33}$$

Generally, the abscissae and weight coefficients of the Gauss-Legendre formula can be computed and tabulated from the equations (32) and (33).
The interval $[-1,1]$ in the Eq.(31) can be transformed into a general finite interval $[V_k, V_{k+1}]$, see Li (2001) and Li & Zhang (2009a). Therefore, the extended Gauss-Legendre quadrature approximation becomes

$$\int_{V_k}^{V_{k+1}} f(V)dV \approx \frac{V_{k+1}-V_k}{2}\sum_{i=1}^{n} A_i f(\frac{V_{k+1}-V_k}{2}t_i + \frac{V_{k+1}+V_k}{2}). \tag{34}$$

To compute the macroscopic flow moments of the distribution function, the discrete velocity domain $[V_a, V_b]$ in consideration can be subdivided into a sum of smaller subdivisions $[V_k, V_{k+1}]$ with N parts according to the thoughts of the compound integration rule, and then the computation of the integration of the distribution function over the discrete velocity domain $[V_a, V_b]$ can be performed by applying the extended Gauss-Legendre formula (34) to each of subdivisions in the following manner.

$$\int_{V_a}^{V_b} f(V)dV = \sum_{k=1}^{N}\int_{V_k}^{V_{k+1}} f(V)dV \ . \tag{35}$$

4. Gas-kinetic numerical algorithm solving the velocity distribution function equation

4.1 Numerical scheme for one-dimensional gas flows

In order to reduce the computer storage requirement, the velocity distribution function equation can be integrated on the velocity components in some directions with appropriate weighting factors, where the components of macroscopic flow velocity are zero. Consequently, the reduced distribution functions can be introduced to cut back the number of independent variables in the distribution function f in the Eq.(15). For problems in one space dimension, say x, a great simplification is possible through the following reduction procedure. Two reduced distribution functions of the x, velocity component V_x and time t are defined, see Chu (1965):

$$g(x,V_x,t) = \int_{-\infty}^{\infty}\int_{-\infty}^{\infty} f(x,V_x,V_y,V_z,t)dV_y dV_z \tag{36}$$

$$h(x,V_x,t) = \int_{-\infty}^{\infty}\int_{-\infty}^{\infty} (V_y^2+V_z^2) f(x,V_x,V_y,V_z,t)dV_y dV_z \tag{37}$$

Now integrating out the V_y and V_z dependence on Eq.(15) in describing one-dimensional gas flows, the following equivalent system to Eq.(15) is got:

$$\frac{\partial g}{\partial t} + V_x\frac{\partial g}{\partial x} = \nu\left(G^N - g\right) \tag{38}$$

$$\frac{\partial h}{\partial t} + V_x\frac{\partial h}{\partial x} = \nu\left(H^N - h\right) \tag{39}$$

Where,

$$G^N = G_M\left\{1+(1-\Pr)(V_x-U)q_x\left[2(V_x-U)^2/T-3\right]\Big/(5PT/2)\right\} \tag{40}$$

$$G_M = n/(\pi T)^{1/2}\exp\left[-(V_x-U)^2/T\right]$$

$$H^N = H_M\left\{1+(1-\Pr)(V_x-U)q_x\left[2(V_x-U)^2/T-1\right]\Big/(5PT/2)\right\} \tag{41}$$

$$H_M = T\cdot G_M$$

The macroscopic flows parameters denoted by the reduced distribution functions can be similarly obtained by substituting Eq.(36) and Eq.(37) into Eqs.(9)~(14).

Thus, the molecular velocity distribution function equation for one-dimensional gas flows can be transformed into two simultaneous equations on the reduced distribution functions instead of one single equation and can be cast into the following conservation law form recurring to the discrete velocity ordinate method described in the Section 3.

$$\frac{\partial \mathbf{U}}{\partial t}+\frac{\partial \mathbf{F}}{\partial x}=\mathbf{S} \tag{42}$$

with

$$\mathbf{U}=\begin{pmatrix} g_\sigma \\ h\sigma \end{pmatrix},\ \mathbf{F}=V_{x\sigma}\mathbf{U},\ \mathbf{S}=\begin{pmatrix} \nu(G_\sigma^N-g_\sigma) \\ \nu(H_\sigma^N-h_\sigma) \end{pmatrix},$$

where g_σ, h_σ, G_σ^N and H_σ^N correspond to the values of g, h, G^N and H^N at the discrete velocity grid points $V_{x\sigma}$, respectively.

Using the NND scheme (Zhang & Zhuang 1992) with the second-order Runge-Kutta method in temporal integral, the finite difference second-order scheme is constructed:

$$\begin{aligned} \delta_t\mathbf{U}^* &= R(\mathbf{U}^n) \\ \mathbf{U}^* &= \mathbf{U}^n+\Delta t\cdot\delta_t\mathbf{U}^* \\ \delta_t\mathbf{U}^{**} &= R(\mathbf{U}^*) \\ \mathbf{U}^{n+1} &= \mathbf{U}^n+\frac{\Delta t}{2}\cdot(\delta_t\mathbf{U}^*+\delta_t\mathbf{U}^{**}) \end{aligned} \tag{43}$$

The operator $R(\mathbf{U}^n)$ is defined by

$$R(\mathbf{U}^n)=-\frac{1}{\Delta x}(\mathbf{H}_{i+1/2}^n-\mathbf{H}_{i-1/2}^n)+\mathbf{S}_i^n$$

with the numerical flux defined by

$$\mathbf{H}_{i+1/2} = \mathbf{F}_i^+ + \frac{1}{2}\min\mathrm{mod}(\Delta\mathbf{F}_{i-1/2}^+, \Delta\mathbf{F}_{i+1/2}^+)$$
$$+\mathbf{F}_{i+1}^- - \frac{1}{2}\min\mathrm{mod}(\Delta\mathbf{F}_{i+1/2}^-, \Delta\mathbf{F}_{i+3/2}^-)$$

and the $\min\mathrm{mod}$ operator is defined by

$$\min\mathrm{mod}(x,y) = \frac{1}{2}[\mathrm{sgn}(x) + \mathrm{sgn}(y)] \cdot \min(|x|, |y|)$$

The stable condition of the scheme can be written as

$$\Delta t_s = CFL \,/\, (\frac{\nu}{2} + \frac{3}{2}\frac{|V_{x\sigma}|}{\Delta x})_{\max} \tag{44}$$

Where CFL is the adjusting coefficient of the time step in the scheme, that is set as $CFL = 0.95$.

Considering the basic feature of the molecular movement and colliding approaching to equilibrium, the time step size (Δt) in the computation should be controlled by coupling the stable condition (Δt_s) of the scheme with the local mean collision time (Δt_c), Bird (1994) and Li & Xie (1996).

$$\Delta t = \min(\Delta t_c, \Delta t_s) \tag{45}$$

Where $\Delta t_c = 1/\nu_{\max}$.

It is well-known that the Euler equations describing inviscid fluid dynamics can be derived from the moments of the Boltzmann or its model equation by setting the velocity distribution function f as a local equilibrium distribution function f_M. In fact, if we consider the Boltzmann model equation and multiply it for the so-called collision invariants of (1, V_x, $V_x^2/2$), by integrating in V_x with the set of a Maxwellian equilibrium state $f = f_M$, we can obtain the Euler equations of the corresponding conservations laws for mass, momentum and energy of inviscid gas dynamics. To catch on the contribution of the collision term to the velocity distribution function and test the capability of the present gas-kinetic numerical method in simulating the Euler equation of inviscid fluid dynamics, it is tested by neglecting the colliding relaxation term in the right of Eq.(42) to substitute the $G_{M\sigma}$ and $H_{M\sigma}$ of the Maxwell equilibrium distribution from the Eqs.(40) and (41) for g_σ and h_σ in the matrix F from the Eq.(42), then the hyperbolic conservation equations can be obtained, as follows

$$\frac{\partial U}{\partial t} + \frac{\partial G}{\partial x} = 0\,, \tag{46}$$

where

$$U = \begin{pmatrix} g_\sigma(x,t) \\ h_\sigma(x,t) \end{pmatrix},\quad G = \begin{pmatrix} V_{x\sigma} G_{M\sigma} \\ V_{x\sigma} H_{M\sigma} \end{pmatrix}.$$

The equation (46) can be numerically solved, and the numerical solution of the Eq.(46) is only the so-called Euler limit solution, see Li & Zhang (2008). Therefore, the gas-kinetic Euler-type scheme is developed for the inviscid flow simulations in the continuum flow regime, illustrated by in the Section 8.1.

4.2 Numerical algorithm for two-dimensional gas flows

For analyses of gas flows in x and y directions around two-dimensional bodies, the molecular velocity distribution function equation in the Eq.(15) can be integrated with respect to V_z with weighting factors 1 and V_z^2 so that the number of independent variables is reduced by integrating out the dependence of f on V_z. The following reduced distribution functions are introduced, see Morinishi & Oguchi (1984); Yang & Huang (1995) and Aoki, Kanba & Takata (1997).

$$g\left(x,y,t,V_x,V_y\right)=\int_{-\infty}^{\infty} f\left(x,y,t,V_x,V_y,V_z\right)dV_z \tag{47}$$

$$h\left(x,y,t,V_x,V_y\right)=\int_{-\infty}^{\infty} V_z^2 f\left(x,y,t,V_x,V_y,V_z\right)dV_z \tag{48}$$

After substituting Eq.(47) and Eq.(48) into the Eq.(15) describing two-dimensional gas flows, and applying the discrete velocity ordinate method to velocity components V_x and V_y, the single velocity distribution function equation can be become into two simultaneous equations with the hyperbolic conservation law form in the transformed coordinates (ξ,η) as follows:

$$\frac{\partial \mathbf{U}}{\partial t}+\frac{\partial \mathbf{F}}{\partial \xi}+\frac{\partial \mathbf{G}}{\partial \eta}=\mathbf{S} \tag{49}$$

with

$$\mathbf{U}=J\begin{pmatrix} g_{\sigma,\delta} \\ h\sigma,\delta \end{pmatrix},\ \mathbf{F}=\bar{U}\mathbf{U},\ \mathbf{G}=\bar{V}\mathbf{U},\ \mathbf{S}=J\begin{pmatrix} \nu(G_{\sigma,\delta}^N-g_{\sigma,\delta}) \\ \nu(H_{\sigma,\delta}^N-h_{\sigma,\delta}) \end{pmatrix},$$

where $g_{\sigma,\delta}$, $h_{\sigma,\delta}$, $G_{\sigma,\delta}^N$ and $H_{\sigma,\delta}^N$ denote values of g, h, G^N and H^N at the discrete velocity points $(V_{x\sigma},V_{y\sigma})$, respectively.

$$G^N=G_M\left[1+(1-\mathrm{Pr})(C_iq_i)\left(2C^2/T-4\right)\Big/\left(5PT/2\right)\right] \tag{50}$$

$$G_M=\frac{n}{\pi T}\exp\left(-C^2/T\right)$$

$$H^N=H_M\left[1+(1-\mathrm{Pr})(C_iq_i)\left(2C^2/T-2\right)\Big/\left(5PT/2\right)\right] \tag{51}$$

$$H_M=TG_M/2$$

$$C^2 = (V_x - U)^2 + (V_y - V)^2$$

$$C_i q_i = (V_x - U) q_x + (V_y - V) q_y$$

Note that $\bar{U}$, $\bar{V}$ are the so-called "contravariant molecular velocity" defined as $\bar{U} = V_{x\sigma}\xi_x + V_{y\delta}\xi_y$, $\bar{V} = V_{x\sigma}\eta_x + V_{y\delta}\eta_y$, J is the Jacobian of the general transformation, that is $J = \partial(x,y)/\partial(\xi,\eta)$. The Jacobian coefficient matrices $A = \partial F/\partial U$ and $B = \partial G/\partial U$ of the transformed Eq.(49) are diagonal and have real eigenvalues $a = \bar{U}$ and $b = \bar{V}$.
In view of the unsteady characteristic of molecular convective movement and colliding relaxation, the time-splitting method is used to divide the Eq.(49) into the colliding relaxation equations with the nonlinear source terms and the convective movement equations. Considering simultaneously proceeding on the molecular movement and colliding relaxation in real gas, the computing order of the previous and hind time steps is interchanged to couple to solve them in the computation. The finite difference second-order scheme is developed by using the improved Euler method and the NND-4(a) scheme (Zhang & Zhuang 1992) which is two-stage scheme with second-order accuracy in time and space.

$$\mathbf{U}^{n+1} = L_s(\Delta t/2) L_\eta(\Delta t/2) L_\xi(\Delta t) L_\eta(\Delta t/2) L_s(\Delta t/2) \mathbf{U}^n \tag{52}$$

Where,

$$\mathbf{U}^* = L_s(\Delta t)\mathbf{U}^n = \mathbf{U}^n + \left(1 - \frac{\nu}{2}\Delta t\right)\Delta t \cdot \mathbf{S}^n \tag{53}$$

$$\mathbf{U}^{**} = L_\eta(\Delta t)\mathbf{U}^* = \left[1 - b\Delta t\delta_\eta + \frac{b^2\Delta t^2}{2}\delta_{\eta^2}\right]\mathbf{U}^* \tag{54}$$

$$\mathbf{U}^{n+1} = L_\xi(\Delta t)\mathbf{U}^{**} = \left[1 - a\Delta t\delta_\xi + \frac{a^2\Delta t^2}{2}\delta_{\xi^2}\right]\mathbf{U}^{**} \tag{55}$$

The integration operator $L_s(\Delta t)$ of the colliding relaxation source terms is done using the improved Euler method. The one-dimensional space operator $L_\eta(\Delta t)$ and $L_\xi(\Delta t)$ of the convective movement terms are approximated by the NND-4(a) scheme. The Δt in the computation can be chosen (Li 2001,2003) as

$$\Delta t = \min(\Delta t_c, \Delta t_s)$$

Here, $\Delta t_s = CFL \Big/ \max(\nu/2, |\bar{U}|/\Delta\xi, |\bar{V}|/\Delta\eta)$.

4.3 Numerical algorithm for three-dimensional gas flows

For the three-dimensional gas flows, the molecular velocity distribution function remains to be a function of seven independent variables in the phase space. The discrete velocity ordinate method can be applied to the velocity distribution function in Eq.(15) to remove its

continuous dependency on velocity components (V_x, V_y, V_z), as described in Section 3.1. Moreover, to treat arbitrary geometry configuration, the body fitted coordinate is introduced. By applying the general transformation technique, Eq.(23) on the discrete velocity distribution functions become in the transformed coordinates (ξ, η, ζ) (Li 2001) as follow:

$$\frac{\partial U}{\partial t} + \frac{\partial F}{\partial \xi} + \frac{\partial G}{\partial \eta} + \frac{\partial H}{\partial \zeta} = S . \tag{56}$$

with

$$U = JQ \ , F = \bar{U}U \ , G = \bar{V}U \ ,$$

$$H = \bar{W}U \ , S = J\bar{S} \ .$$

where

$$\bar{U} = V_{x\sigma}\xi_x + V_{y\delta}\xi_y + V_{z\theta}\xi_z \ , \bar{V} = V_{x\sigma}\eta_x + V_{y\delta}\eta_y + V_{z\theta}\eta_z \ ,$$

$$\bar{W} = V_{x\sigma}\zeta_x + V_{y\delta}\zeta_y + V_{z\theta}\zeta_z \ , J = \partial(x, y, z)/\partial(\xi, \eta, \zeta) \ ,$$

To solve the governing equation (56) at each of $(V_{x\sigma}, V_{y\delta}, V_{z\theta})$ for three-dimensional flow, the time-splitting numerical method can be adopted in the light of the unsteady characteristic of molecular convective movement and colliding relaxation, and the value of U in Eq.(56) at time $n+1$ can be expressed by second-order Taylor series expansion:

$$\begin{aligned} U^{n+1} = & \left[1 - \bar{U}\Delta t\delta_\xi + \frac{\bar{U}^2}{2}\Delta t^2\delta_{\xi^2}\right] \cdot \left[1 - \bar{V}\Delta t\delta_\eta + \frac{\bar{V}^2}{2}\Delta t^2\delta_{\eta^2}\right] \cdot \\ & \left[1 - \bar{W}\Delta t\delta_\zeta + \frac{\bar{W}^2}{2}\Delta t^2\delta_{\zeta^2}\right] \cdot \left[1 - \nu\Delta t(1 - \frac{\nu}{2}\Delta t)\right] U^n \\ & + O(\Delta t^2, \Delta\xi^2, \Delta\eta^2, \Delta\zeta^2) \end{aligned} \ . \tag{57}$$

The above finite difference approximation can be split as the following four operators.

$$U^* = L_S(\Delta t)U^n = U^n + \left(1 - \frac{\nu}{2}\Delta t\right)\Delta t \cdot S^n \ , \tag{58}$$

$$U^{**} = L_\zeta(\Delta t)U^* = \left[1 - \bar{W}\Delta t\delta_\zeta + \frac{\bar{W}^2\Delta t^2}{2}\delta_{\zeta^2}\right]U^* \ , \tag{59}$$

$$U^{***} = L_\eta(\Delta t)U^{**} = \left[1 - \bar{V}\Delta t\delta_\eta + \frac{\bar{V}^2\Delta t^2}{2}\delta_{\eta^2}\right]U^{**} \ , \tag{60}$$

$$U^{n+1} = L_{\xi}(\Delta t)U^{***} = \left[1 - \bar{U}\Delta t\delta_{\xi} + \frac{\bar{U}^2\Delta t^2}{2}\delta_{\xi^2}\right]U^{***}. \tag{61}$$

In fact, the finite difference Eqs.(58)~(61) are respectively consistent with four differential equations in the following,

$$\frac{\partial U}{\partial t} = S, \tag{62}$$

$$\frac{\partial U}{\partial t} + \frac{\partial H}{\partial \zeta} = 0, \tag{63}$$

$$\frac{\partial U}{\partial t} + \frac{\partial G}{\partial \eta} = 0, \tag{64}$$

$$\frac{\partial U}{\partial t} + \frac{\partial F}{\partial \xi} = 0. \tag{65}$$

According to the time-splitting method, on each time interval Δt, a solution of the Eq.(56) is substituted by a solution of a sequence of four Eqs.(62)~(65). Then, the colliding relaxation equation (62) can be numerically integrated by using the second-order Runge-Kutta method:

$$\delta_t U^{*} = \left(1 - \frac{\nu}{2}\Delta t\right)\cdot S(U^n),$$

$$U^{*} = U^n + \Delta t \cdot \delta_t U^{*},$$

$$\delta_t U^{**} = \left(1 - \frac{\nu}{2}\Delta t\right)\cdot S(U^{*}),$$

$$U^{n+1} = U^n + \frac{\Delta t}{2}(\delta_t U^{*} + \delta_t U^{**}). \tag{66}$$

The convective movement equations (63)~(65) in the (ζ, η, ξ) directions of the position space can be numerically solved by using the NND-4(a) finite-difference scheme (Zhang & Zhuang 1992) based on primitive variables, which is a two-stage scheme with second-order accuracy in time and space. For the Eq.(63), the finite-difference scheme can be expressed as

$$U^{*} = U^n - \frac{\Delta t}{\Delta \zeta}(Q^n_{i+1/2} - Q^n_{i-1/2}), \tag{67}$$

$$U^{n+1} = \frac{1}{2}[U^n + U^{*} - \frac{\Delta t}{\Delta \zeta}(Q^{*}_{i+1/2} - Q^{*}_{i-1/2})], \tag{68}$$

$$Q_{i+1/2} = H^{+}_{i+1/2}(U_L) + H^{-}_{i+1/2}(U_R),$$

$$U_{L,i+1/2} = U_{p,i} + \frac{1}{2}\min\mathrm{mod}(\Delta U_{p,i-1/2}, \Delta U_{p,i+1/2}),$$

$$U_{R,i+1/2} = U_{p,i+1} - \frac{1}{2}\min\mathrm{mod}(\Delta U_{p,i+1/2}, \Delta U_{p,i+3/2}),$$

$$\Delta U_{p,i+1/2} = U_{p,i+1} - U_{p,i}.$$

Where, U_p denotes the primitive variable of the Eq.(63), and $H^{\pm}$ respectively denote the flux vector splitters of H based on the positive and negative characteristic values $\lambda^{\pm}$ with $\lambda^{+} = (\lambda + |\lambda|)/2$ and $\lambda^{-} = (\lambda - |\lambda|)/2$. The flux limiter $\min\mathrm{mod}$ operator in the above-mentioned scheme is defined by

$$\min\mathrm{mod}(x, y) = \frac{1}{2}[\mathrm{sgn}(x) + \mathrm{sgn}(y)] \cdot \min(|x|, |y|) \tag{69}$$

Considering simultaneously proceeding on the molecular movement and colliding relaxation in real gas, the computing order of the previous and subsequent time steps is interchanged to couple to solve them in the computation. The second-order finite difference scheme directly solving the six-dimensional discrete velocity distribution functions is set as

$$U^{n+1} = L_S(\frac{\Delta t}{2})L_\zeta(\frac{\Delta t}{2})L_\eta(\frac{\Delta t}{2})L_\xi(\Delta t)L_\eta(\frac{\Delta t}{2})L_\zeta(\frac{\Delta t}{2})L_S(\frac{\Delta t}{2})U^n. \tag{70}$$

In view of the behaviour of the time evolution on the velocity distribution function and the decoupling technique (Bird 1994; Ivanov & Gimelshein 1998 and Li & Xie 1996) on molecular motion and intermolecular collisions in the DSMC method, the time step size (Δt) in the computation should be controlled by coupling the stability condition (Δt_s) of the scheme with the local mean collision time interval (Δt_c), thus we have

$$\Delta t = \min(\Delta t_s, \Delta t_c). \tag{71}$$

with

$$\Delta t_s = \frac{CFL}{\max(\frac{\nu}{2}, \frac{|\bar{U}|}{\Delta\xi}, \frac{|\bar{V}|}{\Delta\eta}, \frac{|\bar{W}|}{\Delta\zeta})}, \Delta t_c = \frac{1}{\nu_{\max}}.$$

Where CFL is the adjusting coefficient of the time step in the scheme, that can be set as $CFL = 0.99$.

For constructing an effective numerical scheme (70) in solving three-dimensional complex flows, the finite difference scheme which approximates the velocity distribution function equation (56) must possess the properties of monotonicity and conservation. The conservative finite-difference schemes are constructed for each separate step in Eqs.(62)~(65), and then the whole scheme is conservative. In the computation of the velocity distribution function, to guarantee the positivity of the distribution function for different Mach number flows, only those discrete velocity ordinate points are considered, at which

the distribution function is greater than a prescribed lower threshold. If at each iteration the time step is fixed according to the condition (71), the scheme (70) is perfectly conservative for mass, momentum, and total energy, and the positivity of the distribution function can be preserved.

5. Gas-kinetic boundary conditions and numerical procedures for the velocity distribution function

Since the present gas-kinetic algorithm explicitly evaluates the time evolution of the molecular velocity distribution function at each of discrete grid points from the physical space and velocity space, all kinds of boundaries should be numerically implemented by directly acting on the velocity distribution function instead of using the macroscopic flow variables. The hyperbolic type of the convective part of the Boltzmann model equation controls and determines the appropriate values of the distribution function in the boundaries. The boundaries can be divided into two parts of Γ_b and Γ_w respectively corresponding to the boundary of the external free flow and to the surface of a body.

5.1 Gas-surface boundary

Thanks to the interaction of the gas molecules with the solid walls, one can trace the origin of the aerodynamics exerted by the gas upon the body and the heat transfer between the gas and the solid boundary Γ_w. The interaction depends on the surface finish, the cleanliness of the surface and its temperature (Cercignani 1994). In general, the interaction of a given molecule with the surface may also depend on the velocity distribution function of molecules impinging on a surface element. Hence it is more convenient to think in terms of a probability density $R(\vec{V} \to \vec{V}';\vec{r})$ (Nocilla 1961.) that a molecule hitting the solid boundary at some point $\vec{r}$ with some velocity $\vec{V}$ reemerges practically at the same point with some other velocity $\vec{V}'$. If R is known, then the boundary conditions for the molecular velocity distribution function $f(\vec{r},\vec{V},t)$ can be easily written down. The general form of the boundary conditions can be written by the aid of the surface balance condition of the mass flux (number of molecules leaving or arriving per unit time and unit area) as

$$\left|\vec{c}'\cdot\vec{n}\right| f(\vec{r},\vec{V}',t) = \int_{\vec{c}\cdot\vec{n}<0} R(\vec{V}\to\vec{V}';\vec{r}) f(\vec{r},\vec{V},t)\left|\vec{c}\cdot\vec{n}\right| d\vec{V}\ ,\ (\vec{r}\in S,\vec{c}'\cdot\vec{n}>0)\ . \tag{72}$$

In view of the difficulty of computing the scattering kernel $R(\vec{V} \to \vec{V}';\vec{r})$ due to the complex physical phenomena of adsorption and evaporation which take place at the wall, mathematical models (Cercignani & Lampis 1971; Kuščer, Možina & Krizanic 1974), that satisfy the basic physical requirements of normalization, positivity and preservation of local equilibrium at the wall, have been proposed. In particular, the scattering kernel corresponding to the Maxwell-type model is used in this paper. By defining the accommodation coefficient which describes how much the molecules accommodate to the state of the wall, the scattering kernel turns out to be

$$R(\vec{V}\to\vec{V}';\vec{r}) = \alpha f_M^w(\vec{V}',\vec{r})\left|\vec{c}'\cdot\vec{n}\right| + (1-\alpha)\delta(\vec{V}'-\vec{V}+2\vec{n}(\vec{c}\cdot\vec{n}))\ ,(\vec{c}'\cdot\vec{n}>0,\vec{c}\cdot\vec{n}<0)\ . \tag{73}$$

According to this model for the scattering kernel, a fraction $(1-\alpha)$ of molecules undergoes a specular reflection, while the remaining fraction α is diffused with the Maxwellian distribution f_M^w of the wall. In general, α turns out to depend on the distribution function of the impinging molecules. A complete accommodation is when the molecules are conserved in number, but otherwise forget completely their impinging distribution. The emerging distribution is then proportional to f_M^w with temperature and mass velocity equal to the temperature and mass velocity of the wall, this gas is in thermal and mechanical equilibrium with the wall. The opposite case with $\alpha = 0$ is when the gas remembers as much as possible of the impinging distribution, then the kernel is a delta function, and all the accommodation coefficients vanish so that the specular reflection is gained,

$$R(\vec{V} \to \vec{V}';\vec{r}) = \delta(\vec{V}' - \vec{V} + 2\vec{n}(\vec{c}\cdot\vec{n})) . \tag{74}$$

In this case, the gas molecules are specularly reflected with the normal component of velocity reversed, therefore the gas cannot exert any stress on the surface, except in the direction of the normal. In fact, if the boundary conditions do not contain the temperature of the wall with the case of a completely reflected gas, then they would allow the gas to stay in thermal equilibrium at any given temperature, irrespective of the surrounding bodies. It is clear that these boundary conditions are quite unrealistic.

In general, the Maxwell-type boundary conditions give satisfactory results with values of α rather close to 1, and in problems where the gas dynamics and momentum transfer are primarily reckoned for the perfect gas without regarding to internal energy transfer, $\alpha = 1$ is a rather accurate assumption. For practical applications, Maxwell's boundary conditions with $\alpha = 1$ are frequently used for the simplicity and reasonable accuracy, and they are a reasonable approximation to any kind of more complicated boundary conditions (Nocilla 1961; Cercignani & Lampis 1971; Kuščer, Možina & Krizanic 1974 and Grad 1949). In all the calculations in this paper, the aforementioned model of gas-surface interaction is implemented and used. According to the condition of the stationary solid wall that no particles penetrate the wall, all molecules striking the solid surface at any time must be reflected back to the gas. If the molecules strike on the surface, the molecular velocity distribution function, which is reflected from the surface, is considered as the form of "drifting Maxwellian" fully accommodating to the wall temperature T_w and velocity (U_w, V_w, W_w), which is set in discretized form as follows:

$$f_{\Gamma_w\sigma,\delta,\theta} = \frac{n_w}{(\pi T_w)^{3/2}} \exp\left[-\frac{(V_{x\sigma} - U_w)^2 + (V_{y\delta} - V_w)^2 + (V_{z\theta} - W_w)^2}{T_w} \right], \vec{c}\cdot\vec{n} \geq 0 . \tag{75}$$

Where $\vec{n}$ is the unit vector normal to the wall surface, pointing to the gas.

The number density of molecules diffusing from the solid surface, n_w, which is not known previously and varied with the velocity distribution of incident molecules and the appearance of the solid surface, can be derived from the insulated condition of zero mass flux normal to the wall surface (Morinishi & Oguchi 1984; Aristov 2001; Li 2001,2003).

$$\int_{c_n>0} c_n f_M^w d\vec{V} = \int_{c_n<0} -c_n f d\vec{V} . \tag{76}$$

Then, substituting the Maxwellian distribution, characterized by the surface temperature T_w, into the left side of the equation (76), one has

$$\frac{n_w}{(\pi T_w)^{3/2}} \iiint_{c_n>0} c_n \cdot e^{-\frac{V_x^2+V_y^2+V_z^2}{T_w}} dV_x dV_y dV_z = \iiint_{c_n<0} -c_n \cdot f dV_x dV_y dV_z \,. \tag{77}$$

As a consequence, the n_w in the preceding reflected distribution function can be obtained

$$n_w = -2\left(\frac{\pi}{T_w}\right)^{1/2} \iiint_{c_n<0} c_n^- \cdot f dV_x dV_y dV_z \,. \tag{78}$$

Where $c_n^- = (c_n - |c_n|)/2$.

If $\vec{c} \cdot \vec{n} < 0$, the discrete velocity distribution functions at the wall grid points of the boundary Γ_w are solved by using second-order upwind-difference approximations from the adjacent grids in the interior of the flow field.

5.2 Outer boundary

The distribution function is assumed to be in equilibrium at infinity. However, the outer boundary Γ_b must be in some finite distance from the body, so the outer boundary conditions are numerically treated using characteristic-based boundary conditions, see Li (2003) and Li & Zhang (2009a,b). These are in accord with the upwind nature of the interior point scheme. From this standpoint, the distribution functions for outgoing molecules through the outer boundary are numerically solved by the second-order finite difference approximation from the interior points, where $\bar{W} > 0$.

For molecules incoming from outside, the characterizing condition $\bar{W} \le 0$ is satisfied for the outer boundary, and the following approximation conditions are used.

1. One can suppose that the condition $\vec{V}_\infty \cdot \vec{n}_b < 0$ is valid along the upstream boundary, where $\vec{n}_b$ is the outward vector normal to the outer boundary and $\vec{V}_\infty$ is the undisturbed free stream velocity, a function describing the undisturbed outer flow is accepted for the part Γ_{b1} of the outer boundary Γ_b ahead of the body, and the distribution functions of the ingoing molecules are set as the local equilibrium distribution with prescribed free stream properties. As a rule, the equilibrium distribution function for the molecules directed into the domain of the flow field is imposed for points of the free boundary surface Γ_{b1} in discretized form as follows

$$f_{\Gamma_{b1}\sigma,\delta,\theta} = f_{M\sigma,\delta,\theta} \cdot \left[1 + (1-\mathrm{Pr})\vec{c}_{\sigma,\delta,\theta} \cdot \vec{q}\left(2c_{\sigma,\delta,\theta}^2/T - 5\right)/\left(5PT/2\right)\right], \tag{79}$$

$$f_{M\sigma,\delta,\theta} = n/(\pi T)^{3/2} \exp\left[-c_{\sigma,\delta,\theta}^2/T\right], \tag{80}$$

where n, T, P, $\vec{U}$ are density, temperature, pressure and the vector of mean velocity of undisturbed gas flow.

2. For the other part Γ_{b2} of the free boundary surface Γ_b, where $\vec{V}_\infty \cdot \vec{n}_b \ge 0$ in the downstream boundary, it is assumed that there is no gradient along the outward ς – direction for the distribution functions, which is, for incoming molecules,

$$\frac{\partial \Delta U}{\partial \zeta} = 0 \quad \text{for} \quad \bar{W} \le 0\,, \quad \vec{V}_\infty \cdot \vec{n}_b \ge 0\,. \tag{81}$$

6. Parallel implementation of the gas-kinetic algorithm for three-dimensional complex flows

It can be shown from the present gas-kinetic algorithm that the discrete velocity ordinate method needs to be employed to discretize the molecular velocity space to cast the velocity distribution function equation into hyperbolic conservation equations with nonlinear source terms, and then the finite difference method from computational fluid dynamics is developed to numerically solve the velocity distribution functions at each of discrete velocity ordinate points. For the computation of three-dimensional flow problems, the six-dimensional array needs to be used to access the velocity distribution functions at all points in the discrete velocity space and physical space, so a great deal of computer memory is needed. It is impractical relying on current serial computer for the present gas-kinetic algorithm to attack three-dimensional complex hypersonic flows. On the other hand, it has been indicated from the computational procedure of the algorithm that the direct computation of time evolution of the velocity distribution function over the velocity space and physical space can be split up into two parts, one is that the discrete velocity distribution functions are solved by the gas-kinetic numerical schemes described in Section 4.3 independently and concurrently at every given discrete velocity ordinate point, the other is that macroscopic flow parameters at each point of the physical space are evaluated by the discrete velocity numerical integration methods described in Section 3.2. The essential and important feature of the above-mentioned computation strategy is that the calculations in the velocity space can be uncoupled from those in the physical space without any communication connection, which makes the gas-kinetic algorithm well suitable for parallelizing. To resolve the difficulty of the vast computer memory needed by the current method in solving three-dimensional complex flows and to well exploit massive power of parallel computers, the multi-processing strategy and parallel implementation technique suitable for the gas-kinetic numerical algorithm are investigated using the technique of domain decomposition, see Li (2003) and Li & Zhang (2009a,b).

The computing space of the gas-kinetic algorithm for three-dimensional flow problems relates to the six-dimensional phase space consisting of the discrete velocity space (σ,δ,θ) and physical space (i,j,k), however, none but the velocity distribution function under consideration is defined in the six-dimensional space, other variables or modules of the algorithm are merely defined in the subspace of (i,j,k) or (σ,δ,θ) so that good data-parallel independency exists in the gas-kinetic algorithm. In practical computation, the bounds of the discrete velocity space are wide especially for hypersonic flow problems so that the number of discrete velocity grid points $N_\sigma \times N_\theta \times N_\delta$ needed could become quite large, as is specially suitable for the decomposing strategy of discrete velocity space Ω_V. For the decomposing strategy of Ω_V, as the computing quantity of the reduced summation spent on the moments of the distribution function is only under $1/5$ of the whole computing workload of the algorithm, the number of parallel processors can reach up to the maximum number of $N_\sigma \times N_\theta \times N_\delta$ so that the parallel scalability of up to 1000 processors can be effectively realized. Considering that the computing process of the gas-kinetic

algorithm possesses good peculiarity of data parallel, the discrete velocity mesh (σ,δ,θ) will be distributed over the parallel processors in the block-layout manner. To enhance the parallel efficiency, the parallelized loops of σ,δ,θ are adjusted outside the loops of physical coordinates (i,j,k), in this way, the data communication time arisen from the reduced summation during the calculation of macroscopic flow parameters is greatly reduced down to $i_{\max}\times j_{\max}\times k_{\max}$ times. It is found from the parallelizing implementation on the present gas-kinetic algorithm that the workload assigned to each processor for the numerical computation of the $f_{\sigma,\delta,\theta}$ is the $1/n$ of the total computation load, and the size of the distributed memory of each CPU is also the $1/n$ of the total amount of memory in handling the calculation of three-dimensional problems, as so makes it practicable that the problems unsolved under the limitation of serial computer memory can be solved by concurrent computation with high parallel efficiency and speed-up ratio. In this study, the parallel code adapted to the present method has been developed and applied to solve hypersonic flows around three-dimensional complex body under the parallel environment offered by the parallel multi-computer system from the Parallel Computing Research Center in Beijing.

7. Efficiency and convergence of the gas-kinetic unified algorithm

For the computational procedure of the present gas-kinetic algorithm, after the physical and velocity space are discretized and the initial condition of the flow field is set, the finite-difference scheme given in Section 4 is used to numerically solve the discrete velocity distribution functions with the use of the gas-kinetic boundary conditions, see Li (2003) and Li & Zhang (2004a,b). Then, the macroscopic flow parameters at each of points of the physical space are evaluated with the discrete velocity quadrature methods. After the above procedures are finished with the renewed correction of the velocity distribution function equation, the process of the computation of the distribution function for the new time level will be repeated. The iterative procedure is stopped when the quadratic global relative error of the flow quantities (e.g. density, flow velocity, temperature) between successive iteration steps is less than 10^{-5}.

It can be shown from the present gas-kinetic algorithm that the discrete velocity ordinate method needs to be employed to discretize the molecular velocity space to cast the velocity distribution function equation into hyperbolic conservation equations with nonlinear source terms, and then the finite difference method from computational fluid dynamics is developed to numerically solve the velocity distribution functions at each of discrete velocity ordinate points. The numerical accuracy of the gas-kinetic algorithm can be verified by the performance of the physical models, the accuracy of the discrete velocity ordinate method, the numerical precision of the finite difference scheme, and the grid convergence from the velocity space and physical space. As a model form of the Boltzmann equation, the simplified velocity distribution function equation relied by the algorithm is used to describe the molecular transport phenomena from various flow regimes. It is not exact as the original Boltzmann equation, but reliable to qualitatively describe gas flows from various regimes, even as is described in Li (2001); Li & Zhang (2007,2008,2009a,b). The accuracy of the discrete velocity ordinate method mostly rests with the relevant discrete velocity numerical quadrature technique and the size of the discrete velocity domain. Only when the number of the discrete velocity ordinate points goes up to infinity, the numerical integration may

exactly approach the original integral moment. However, the increase of the relevant discrete velocity ordinate points always brings about the need of more computer memory. Then, the discrete velocity numerical quadrature method consequentially has a finite truncation error. In the computation, the appropriate discrete velocity numerical quadrature and the discrete velocity domain for the velocity space should be selected for more accuracy by one order than the required precision of the global computation. In addition, the numerical accuracy in solving the discrete velocity distribution functions principally depends on the adoptive finite-difference scheme, here, the NND scheme is employed to discretize the convective terms in physical space which is second-order accurate in time and space with the fast convergence speed, and the second-order Runge-Kutta method is used to solve the colliding relaxation equations with the non-linear source terms. The characteristic-based boundary conditions which are in accord with the upwind nature of the interior point scheme are developed in the present algorithm. Since the interior scheme of the second-order accuracy is used, the characteristic-based second-order upwind boundary scheme may be accurate enough to retain the second-order global accuracy in the physical space. Generally, the grid is finer, and the numerical accuracy is better. It has been shown from the computing practice (Li 2003; Li & Zhang 2004a,b) that the results of the present method are not sensitive to the grid spacing in the physical space or the velocity space if only the required precision in the computation can be satisfied. The present method is very stable and robust without the limitation of the cell size, even when the grids are coarse, and the computation still is convergent rapidly to the required numerical precision. Figure 1 describes the convergent curve of the present unified algorithm in solving sphere flows, where the vertical-axis denotes the quadratic global residual error of the macroscopic flow quantities and the horizontal abscissa denotes the computing iterative times in the marched time. It can be shown from Fig.1 that the computation is very stable and convergent with the fast converging speed even though the coarse grid system is used with $25 \times 17 \times 21$ in the physical space.

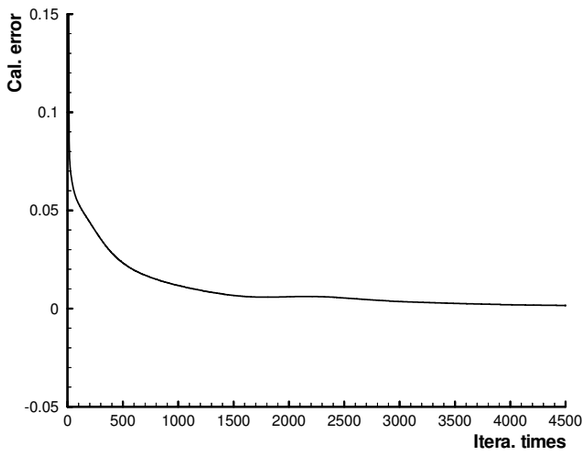

Fig. 1. Converging curve of the present algorithm

The present gas-kinetic algorithm is well competent for solving the gas flows covering various flow regimes, especially in the near-continuum and rarefied transitional flows. It has been shown from the computation that the computer time required for the present method increases as the Knudsen number decreases. In the computation of the continuum flow, as

the molecular mean collision time is generally smaller than the time step determined by the stable condition of the finite difference scheme, then the computing time step given by eq.(71) will be quite little at the magnitude of 10^{-5}, as a result, the convergent speed of the present method seems be slower than that of the Navier-Stokes solver for the continuum flow regime, especially in the computation of three-dimensional continuum flows. In addition, since a great deal of computer memory is needed to store the discrete velocity distribution functions at each of points in the discrete velocity space and physical space, the computations of the one- and two-dimensional flows can be realized in the microcomputers, however, the careful computations of three-dimensional flows with high Mach numbers have to be operated by the parallel computing on a large scale.

8. Study of gas flows covering various flow regimes

To test the accuracy and efficiency of the present numerical method in solving the gas dynamical problems from rarefied flow to continuum, the gas-kinetic numerical algorithm developed in the foregoing sections will be used to study the complex gas flows and aerodynamic phenomena with different Mach numbers including the one-dimensional shock-tube and normal shock-structure problems, the flows past two-dimensional circular cylinder and the flows past three-dimensional sphere and spacecraft shape with various Knudsen numbers, in which the one-dimensional and two-dimensional problems are studied by the serial computation, and the three-dimensional complex flows are studied by HPF parallel computing.

8.1 One-dimensional shock-tube problems with various Knudsen numbers

The unsteady shock-tube problems are usually used as one of standard examples of one-dimensional gas flows to validate the numerical methods. It can be described by the way where a diaphragm located at $x = 0.5$ divides a one-dimensional flow field into two regions, each in a constant equilibrium state at $t = 0$.

8.1.1 Unsteady Riemann shock-tube problem

The Riemann shock-tube problem, which has been numerically studied by Chu (1965); Reitz (1981); Prendergast & Xu (1993) and Xu (1998) etc. is considered with initial states:

$$0.0 \le x \le 0.5 : \rho_L = 0.445, T_L = 13.21, U_L = 0.698 ,$$

$$0.5 < x \le 1 : \rho_R = 0.5, T_R = 1.9, U_R = 0.0 .$$

Figs.2(a)~(c) respectively show the pressure, temperature and flow velocity distribution at time $t = 0.1314$ with different Knudsen numbers from continuum to rarefied flow regimes, where the solid lines are obtained from the Riemann exact solutions of inviscid gas dynamics, the symbols (o) denote the computed Euler limit solutions of continuum flow from the gas-kinetic scheme of Eq.(46), the symbols (Δ) denote the computed results related to the continuum flow state with the viscosity coefficient of $\mu_{ref} = 0.0005$, the symbols (∇) denote the computed results related to the near-continuum flow of $Kn = 0.005$, the symbols ($\triangleright$) denote the computed results for the transition regime with $Kn = 0.01$, and the symbols ($\Diamond$) denote the computed results related to the high rarefied flow of $Kn = 0.1$.

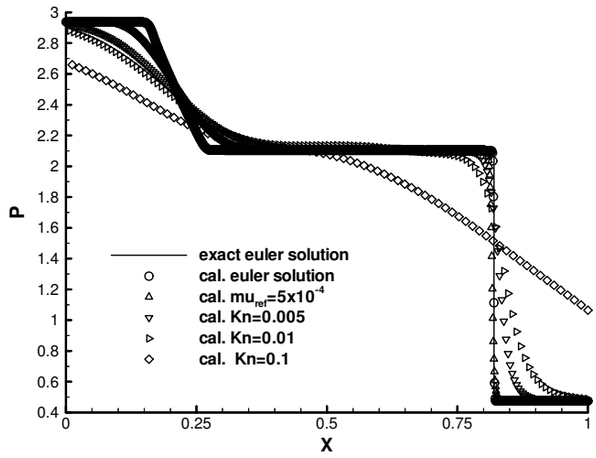

(a). Pressure

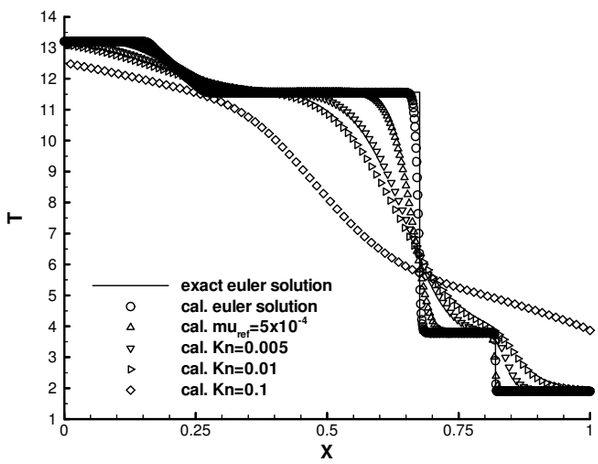

(b). Temperature

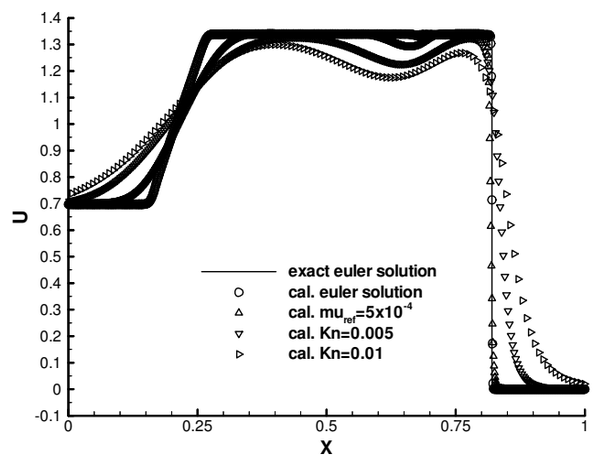

(c). Flow velocity

Fig. 2. Pressure, temperature, flow velocity distribution of Riemann shock-tube problem as a function of x with different Knudsen numbers at $t = 0.1314$.

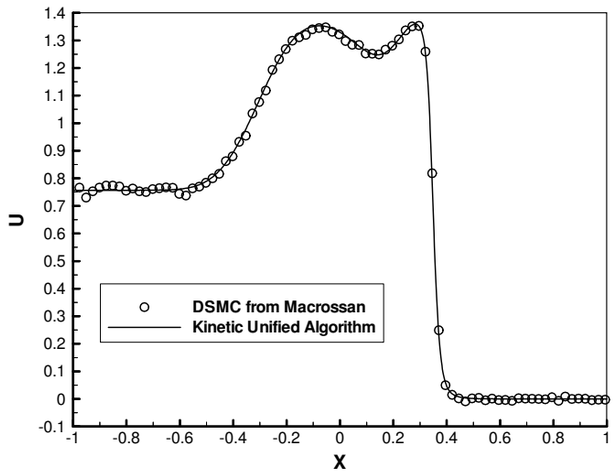

Fig. 3. Flow velocity profiles of the Riemann shock-tube flow for the case of $Kn = 0.005$ at $t = 0.13$ with the present computation and the DSMC results.

It's shown that the excellent agreement is observed between the present computed Euler limit solutions and the Riemann exact solutions. With the increase of the Knudsen number, the shock and rarefaction waves get thicker so that the rarefied flow corresponding to $Kn = 0.1$ only exists in some disturbance without the shock, contact or rarefaction waves, however, for the continuum flow related to $\mu_{ref} = 0.0005$ and the Euler limit solutions, the crisper shock and rarefaction wave profiles are given. Figs.2(a)~(c) qualitatively reveal the non-equilibrium changing process from various flow regimes that the gas flow becomes from rarefied flow to continuum along with diminishing the Knudsen number from $Kn = 0.1$ to tiny value. In particular, Fig.2(c) shows a peculiar non-equilibrium phenomenon of rarefied gas flow that the computed flow velocity near the contact discontinuity surface deviates from the exact solution of inviscid gas dynamics, the deviation becomes more prominent with the increase of Knudsen number, and the deviation gradually vanishes when the flow comes into the continuum flow. The curious and interesting deviation near the contact surface may be induced from the conservation of the total momentum in the shock tube. For rarefied flow, the molecular velocity distribution remarkably deviates from the Maxwellian distribution, and the shock and rarefaction waves become thick. To conserve the mass and momentum in the tube for any Knudsen number flow, the area under the computed velocity profiles should be the same as the area under the profiles of the exact continuum solutions, any asymmetric deviation from the continuum solutions in the shock or the expansion wave profile must necessarily appear as a deviation in the region near the contact discontinuity surface. Only when the Knudsen number becomes small and the gas comes into being the continuum flow, the velocity distribution function f approximatively or completely becomes into the Maxwellian distribution, then the velocity value should be equal in both sides of the contact discontinuity surface. To further validate this non-equilibrium phenomenon of the deviation from the equilibrium value in the flow velocity profiles, the quantitative comparison between the present computation and the DSMC results from Prof. M. Macrossan from School of Engineering in University of Queensland has been made in Fig.3. This figure presents the flow velocity distribution of the Riemann

shock-tube flow for the case of $Kn = 0.005$ at time $t = 0.13$ with two results from the present computation and the DSMC simulation, where the initial state is set as $\rho_L = 0.89$, $T_L = 6.9526$, $U_L = 0.7566$ for $-1 \le x \le 0$, and $\rho_R = 1$, $T_R = 1$, $U_R = 0$ for $0 < x \le 1$. It's shown from Fig.3 that the present computation smoothly and accurately reveals the non-equilibrium deviation of rarefied gas effect in the velocity profiles, and the present computation is found in good agreement with the DSMC results.

8.1.2 SOD shock-tube problem

In order to further test the gas-kinetic numerical algorithm and show the effect of rarefaction in the shock tube flow with various Knudsen numbers, the shock-tube Sod problem is set with the initial condition,

$$0.0 \le x \le 0.5 : \rho_L = 10.0, T_L = 1.667, U_L = 0.0 ,$$

$$0.5 < x \le 1 : \rho_R = 1.0, T_R = 1.333, U_R = 0.0 .$$

Fig.4(a) and Fig.4(b) respectively show the computed results of density and flow velocity distribution at time $t = 0.1912$ for the cases of $Kn = 0.1$, 0.01, 0.005 and $\mu_{ref} = 0.0005$ with the comparisons between the computed Euler limit solutions from Eq.(46) and the exact solutions obtained using the Euler equations of gas dynamics of continuum flow. It can be observed that the distinct rarefaction, contact and shock wave are gradually formed along with the reduction of the Knudsen number from $Kn = 0.1$ to $Kn = 0.005$, and the computed profiles related to the continuum flow of $\mu_{ref} = 0.0005$ approach to the exact solutions of the continuum flow, especially, the computed Euler limit solutions is in excellent agreement with the Euler limit solutions of inviscid gas dynamics. There isn't shock and expansion wave, but only exists in strong disturbance for the rarefied flow related to $Kn = 0.1$.

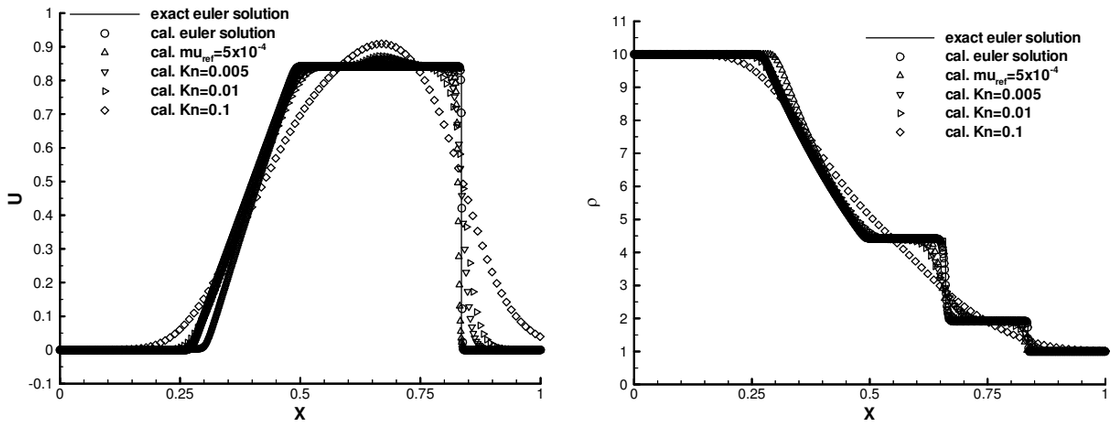

(a). Density (b). Flow velocity

Fig. 4. Density and flow velocity distribution of shock-tube Sod problem with different Knudsen numbers at $t = 0.1912$ for the cases of the exact solution of the Euler equations (Solid line), the computed Euler limit solution (o), the computed continuum solution (Δ) related to the viscosity coefficient of $\mu_{ref} = 0.0005$, the computed results (∇) of near-continuum flow with $Kn = 0.005$, and the computed results corresponding to rarefied flow with $Kn = 0.01$ (▷) and $Kn = 0.1$ (◊).

In Fig.4 (b), the bump phenomena of non-equilibrium deviation of rarefied gas effect can be similarly shown near the contact discontinuity surface, this bump becomes more prominent with the increase of Knudsen numbers. The above-mentioned numerical analysis demonstrates that the rarefied gas effect, viscosity and diffusivity of gas molecules are different from various flow regimes, which induces the notable difference of flow characteristic from rarefied to continuum flow regimes.

8.2 Normal shock-structure problems for different Mach numbers

The internal structure of a plane normal shock wave involves the transition from a supersonic upstream flow to a subsonic downstream flow and provides an important test case for the verification of numerical methods. Shock waves are characterized by their upstream Mach number of $M_s = U_1/a_1$, where U_1 and $a_1 = \sqrt{\gamma RT_1}$ are the flow velocity and sound speed at the upstream equilibrium state. The flow is initialized with two Maxwellian equilibrium states related by classical Rankine-Hugoniot relations. In addition, the steady state of a shock wave shows the transition between upstream and downstream flows. The profiles of shock waves take on different transport properties for strong and weak shock with different Mach numbers, in particular, the flow of shock structures with a Mach number less than two is almost in the continuum or near-continuum regime, however, the internal structure of shock waves with a higher Mach number appears as having rarefied flow character. In the following computation, the density is normalized as $(\rho - \rho_1)/(\rho_2 - \rho_1)$ in terms of the densities ρ_1 and ρ_2 in the upstream and downstream of the shock wave, and the normalized values of the temperature are defined in a similar manner. The length scale is normalized as x/λ_1 by the mean free path (λ_1) of the upstream flow, where the origin is set at the point in the profile where the density is midway between the upstream and downstream values. To describe the non-equilibrium flow properties in the interior of a normal shock wave and demonstrate the reliability of the present algorithm in solving the shock structure problems for different Mach numbers, the cases of $M_s = 1.2$, 1.4, 2, 3.8, 8, 9, 10 for argon gas have been computed with $\Pr = 2/3$, $\gamma = 5/3$, where the properties under standard conditions for argon gas are employed from Appendix A in Bird (1994).

8.2.1 Numerical test of shock structures

Fig.5 respectively shows the computed profiles of density and temperature for the cases of $M_s = 1.2$, 1.4 and 2 corresponding to the viscosity-temperature index $\chi = 0.81$ with the comparison of the continuum Navier-Stokes solutions from Gilbarg & Paolucci (1953) and the DSMC results from Bird (1994).

As shown from Fig.5 (a), for the very weak wave of $M_s = 1.2$, the present gas-kinetic solutions are in excellent agreement with the N-S prediction and the DSMC results, however, the statistical scatter is outstanding for the DSMC method to capture such a small disturbance with the density ratio of 1.2973. It can be observed from Fig.5(b) corresponding to $M_s = 1.4$ that three sets of results generally accord well with one another, however there is a significant discrepancy in the density profiles from the predictions of the Navier-Stokes equations occurred in the downstream half of the shock wave. For the case of $M_s = 2$, two sets of results from the present algorithm and DSMC method are in good agreement, but the

N-S solutions are seriously deviated from the DSMC simulation and the present computation so that the continuum N-S predictions seem to be invalid for shock Mach numbers greater than two, which confirms studies of weak shock wave from Pham-Van-Diep, Erwin & Muntz (1991) and Bird (1984). On the other hand, it can be validated from Fig.5 that there is a prominent increase in the separation between the temperature and density profiles with the higher shock Mach numbers from $M_s = 1.2$ to $M_s = 2$, which manifests that the normal shock wave is a non-equilibrium flow with large departures from thermodynamic equilibrium.

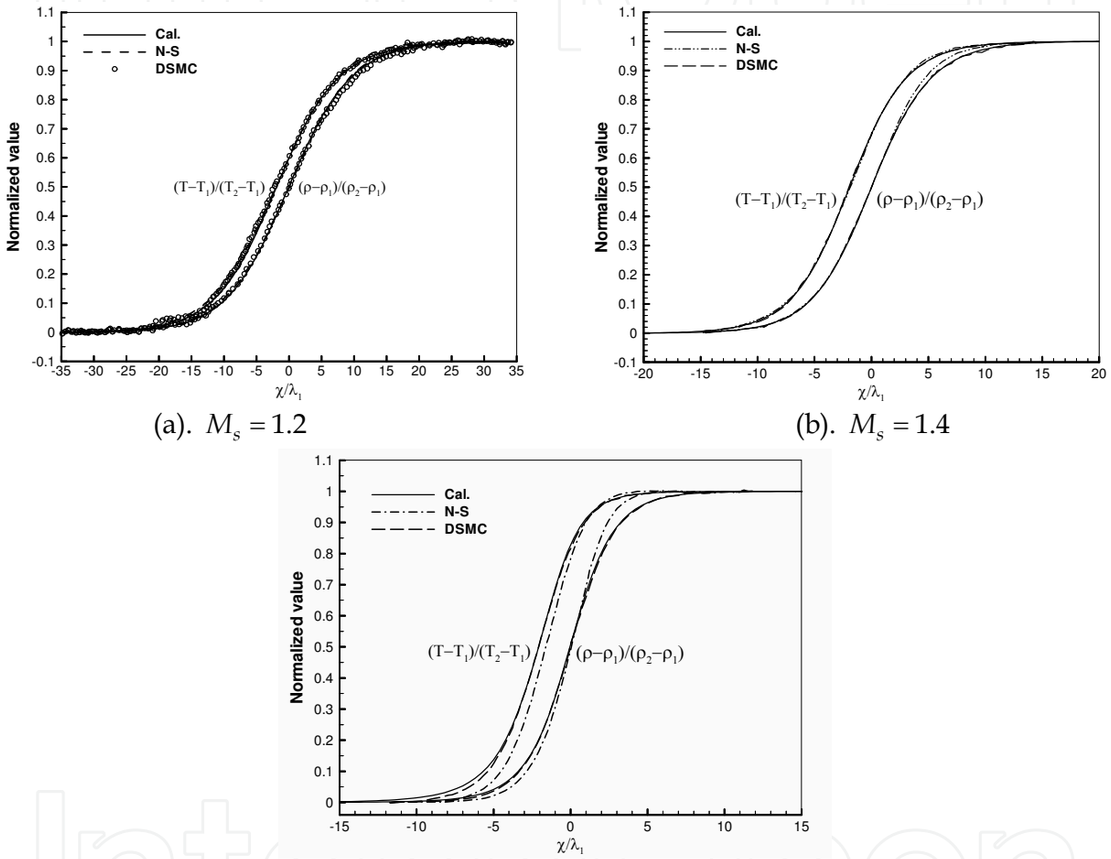

(a). $M_s = 1.2$ (b). $M_s = 1.4$

(c). $M_s = 2$

Fig. 5. Computed temperature and density profiles of shock structure with DSMC results and N-S prediction for the cases of $M_s = 1.2$, 1.4 and 2.

Corresponding to the structures of moderate and strong shock waves for the cases of $M_s = 3.8$ and $M_s = 9$, the present computed results for $\chi = 0.72$, as well as the experiment data from Alsmeyer (1976), the DSMC simulation from Bird (1970) and the solutions of the Mott-Smith theory (Muckenfuss 1962), are shown in Fig.6, respectively.

The figure clearly shows that the present gas-kinetic solutions of the shock profiles for both the intermediate Mach number $M_s = 3.8$ and the high Mach number $M_s = 9$ are in good agreement with the experiment data and DSMC results. It can be shown that the Mott-Smith moment method fits well to describe the density distribution for the structure of shock

waves, however, it is difficult to give the temperature distribution since temperature is a more sensitive quantity as a higher moment of the velocity distribution function, and the Mott-Smith theory is better for lower than for higher Mach number flow. It can be confirmed from the present computations described in Fig.5 and Fig.6 over the whole range of Mach numbers from $M_s = 1.2$ to $M_s = 9$ that the density profiles are nearly symmetric on the point of the intermediate density between the upstream and downstream states, however, as the shock becomes stronger, some qualitative changes different from the weak shock waves appear in the strong shock profiles shown in Fig.6, that is, a marked asymmetry and overshoot phenomena has arisen in the temperature profiles. The asymmetry and prominent augment are more remarkable for higher Mach numbers from $M_s = 3.8$ to $M_s = 9$, as reveals the severe rarefied non-equilibrium effect existing in the strong shocks.

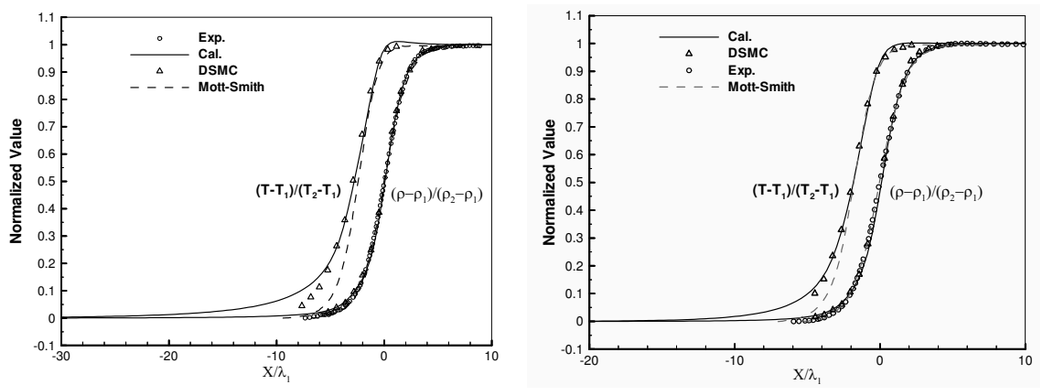

(a). $M_s = 3.8$ (b). $M_s = 9$

Fig. 6. Shock wave profiles of temperature and density with the comparison of the present computation and the DSMC results, Mott-Smith moments, and experimental data for the cases of $M_s = 3.8$ and 9.

8.2.2 Non-equilibrium velocity distribution in the interior of normal shock wave

In this section, the behavior of the velocity distribution function in the interior of steady normal shock wave is described by the present gas-kinetic numerical method. Figures 6~8 show the non-normalized distribution function g of Eq.(36) as the function of the velocity component of V_x/c_{mref} at different locations of $x/\lambda_1 = -20, -10, -5, 0, 10$ within the shock wave for the cases of $M_s = 1.4$, 3.8 and 8. For the inner flow of the shock wave with low Mach number of $M_s = 1.4$, it can be observed from Fig.7 that the velocity distribution almost takes on the standard form of the Maxwellian equilibrium distribution at any situations of shock structure. For the shock structure of the intermediate Mach number $M_s = 3.8$, the velocity distribution function plotted in Fig.8 is different from the velocity distribution corresponding to the weak wave of $M_s = 1.4$, especially near by the central location of $x/\lambda_1 = 0$, the velocity distribution holds a long trail of the non-equilibrium distribution in the negative direction of the axial velocity, however, when the flow is at equilibrium (upstream and downstream), the dependent relation of the velocity distribution function on the axial component of velocity almost pertains to the symmetric form of the

Maxwellian distribution, such as at locations of $x/\lambda_1 = -20, -10, -5$ closely in the front of the shock wave and $x/\lambda_1 = 10$ behind the shock wave.

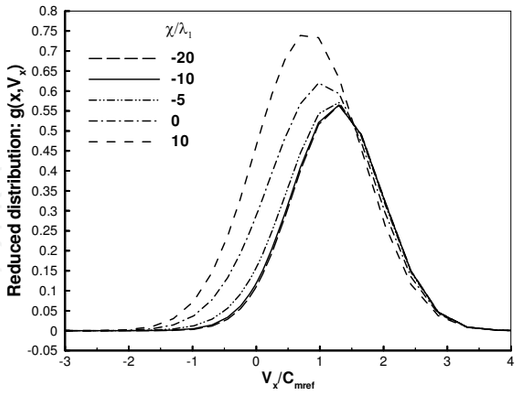

Fig. 7. Computed profiles of the axial velocity distribution function at different locations of $x/\lambda_1 = -20, -10, -5, 0, 10$ within the shock wave for $M_s = 1.4$.

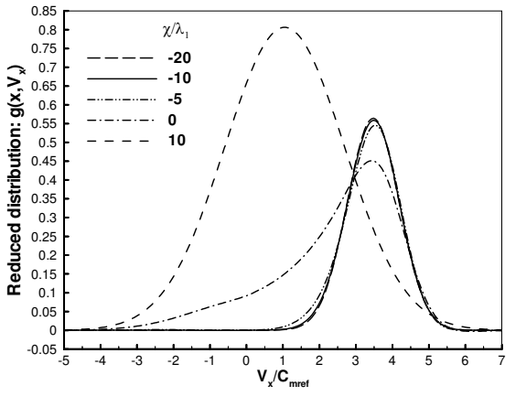

Fig. 8. Computed profiles of the axial velocity distribution function at different locations of $x/\lambda_1 = -20, -10, -5, 0, 10$ within the shock wave for $M_s = 3.8$.

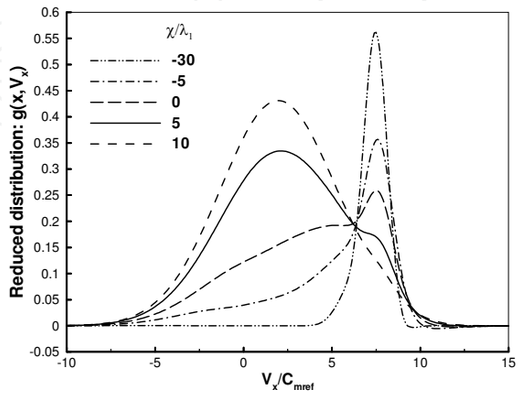

Fig. 9. Computed profiles of the axial velocity distribution function at different locations of $x/\lambda_1 = -30, -5, 0, 5, 10$ within the shock wave for $M_s = 8$.

Fig.9 exhibits the velocity distribution of g as the function of the axial component of velocity for the strong shock wave with the high Mach number of $M_s = 8$ at different locations of $x/\lambda_1 = -30, -5, 0, 5, 10$. It can be shown from Fig.9 that the molecular velocity distribution appears as the essentially non-equilibrium form across the inner flow of the shock structure, the distribution function at the center of the shock wave seems to present the complete non-equilibrium distribution with the long tail similar to bimodal distribution. The severe departure from equilibrium of the distribution function reflects the extreme non-equilibrium effect existed in the interior of the shock structure. Figs.7~9 exhibit that the gas flow becomes from the small deviation from local equilibrium to the highly non-equilibrium when the shock Mach number change from $M_s = 1.4$ to $M_s = 8$.

8.2.3 High moments of heat flux and stress within the shock structures

In order to further validate the capability of the gas-kinetic algorithm in computing the higher-order macroscopic moments of the velocity distribution function, the heat flux vector q_x and the viscous shear stress τ_{xx} from the present computation for the strong shock flow of $M_s = 8$ are shown in Figs. 10 and 11 with the comparison of the continuum Navier-Stokes prediction and the DSMC simulation in Bird (1970), where the vertical ordinate denotes the negative value of heat flux in the $x-$direction, the heat flux q_x has been normalized by dividing by the product of the density and the cube of the most probable velocity in the undisturbed gas, and the viscous shear stress τ_{xx} has been normalized by dividing by the product of the density and the square of the most probable velocity.

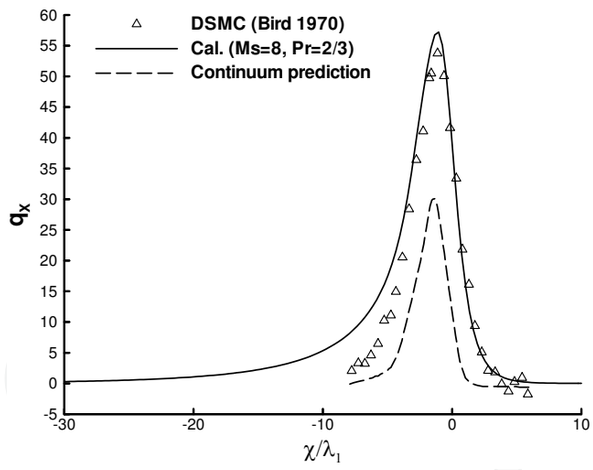

Fig. 10. Computed heat flux profiles in the interior of the shock wave with DSMC results and N-S prediction for $M_s = 8$.

From Figs.10 and 11, it can be distinctly revealed that the profiles of heat flux and viscous stress possess the remarkable asymmetric distribution based on the centre of the wave, and the agreement between the DSMC results (Symbols Δ) and the present computation (Solid line) can be obtained where some differences exist in the front of the shock wave with more prominent non-equilibrium distribution from the present computation, however, a severe deviation exists in the results of the continuum Navier-Stokes prediction (Dashed line),

especially the prediction of heat flux distribution is poor so that the macroscopic continuum theory based on the Chapmann-Enskog expansion of the Maxwellian equilibrium distribution have difficulty in describing higher-order flow moments of the distribution function. To see the variation of the viscous stress and heat flux inside the shock structures at different Mach numbers, Figs.12(a) and (b) respectively illustrate the heat flux and viscous stress profiles in the $x-$direction for the cases of $M_s = 3.8$, 9 and 10, where the Dash-Dot-Dot line denotes the computed results for $M_s = 3.8$, the Dashed line relates to the computed results for $M_s = 9$, and the Solid line denotes the computed results for $M_s = 10$.

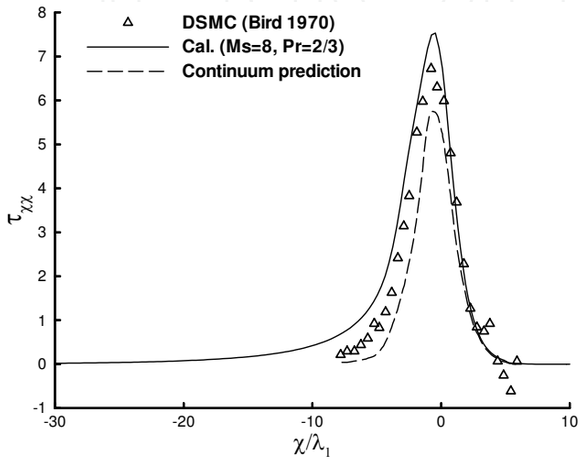

Fig. 11. Computed viscous stress profiles in the interior of the shock wave with DSMC results and N-S prediction for $M_s = 8$.

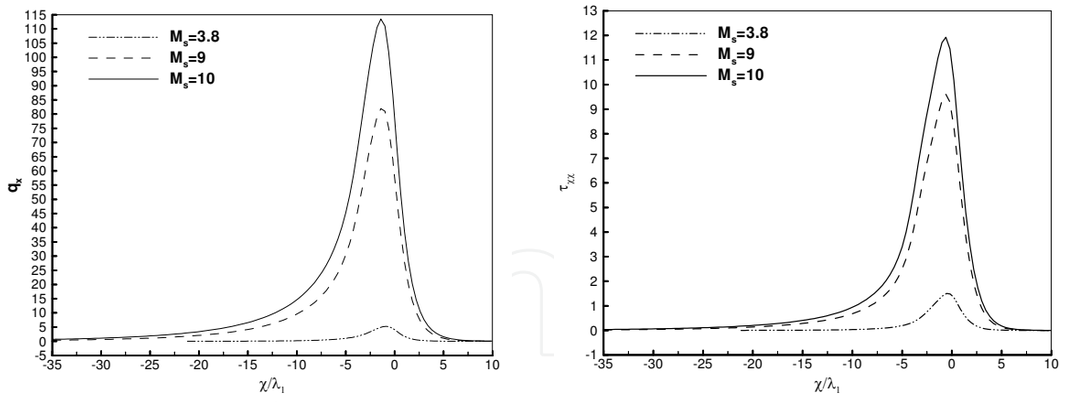

(a). Heat flux (b). Viscous stress

Fig. 12. Heat flux and Viscous stress distribution of the shock structure with different Mach numbers of $M_s = 3.8$, 9, 10.

It can be shown from Fig.12 that as the shock Mach number increases, the heat flux and viscous stress quantities go up rapidly, and the peak of the profiles is far from the centre of the wave with strong rarefied non-equilibrium effect. For the intermediate Mach number ($M_s = 3.8$) shock structure, the profiles of the viscous stress and heat flux only have a small deviation from the symmetric equilibrium distribution based on the center of the wave. For

the high Mach number ($M_s = 9$ and $M_s = 10$) shock flow, the prominent asymmetric distribution appears in the profiles, the significant increase in the heat flux is accentuated by a region in the front of the wave.

8.3 Two-dimensional supersonic flows past cylinder from rarefied regime to continuum

The steady supersonic flows past a circular cylinder under various free-stream Mach (M_∞) and Knudsen numbers are computed. Here, due to symmetry, only half plane on the cylinder is considered and symmetry boundary conditions were employed. The mesh system used is 71×51 (streamwise $\times$ surface normal) in the physical space and the modified Gauss-Hermite quadrature formula with 32×32 discrete velocity ordinate points was employed. The computational results of the pressure and Mach number contours are shown in Fig.13 and Fig.14, respectively, respected to the states of $M_\infty = 1.8$, $\Pr = 2/3$, $\gamma = 5/3$, the ratio $T_w / T_0 = 1$ of the wall temperature to the total temperature, $Kn = 1$, 0.1 , 0.03 and $Kn = 0.001$ ($M_\infty = 4$) . It's shown in Fig.13 and Fig.14 that there is no shock wave disturbing region for the fully rarefied flow related to $Kn = 1$, however, the strong disturbing domain and the dim bow shock appear in the rarefied transition flows related to $Kn = 0.1$ and $Kn = 0.01$, and for the near continuum flow of $Kn = 0.001$, the flow structures including the front bow shock, stagnation region and near wake are well captured. The smaller is the Knudsen number, the thinner and clearer is the bow shock occurring in front of the body. It's shown from Fig.13-Fig.14 that the gas flow approaches to continuum flow from rarefied transition flow while the Knudsen number is diminishing from $Kn = 1$ to $Kn = 0.001$.

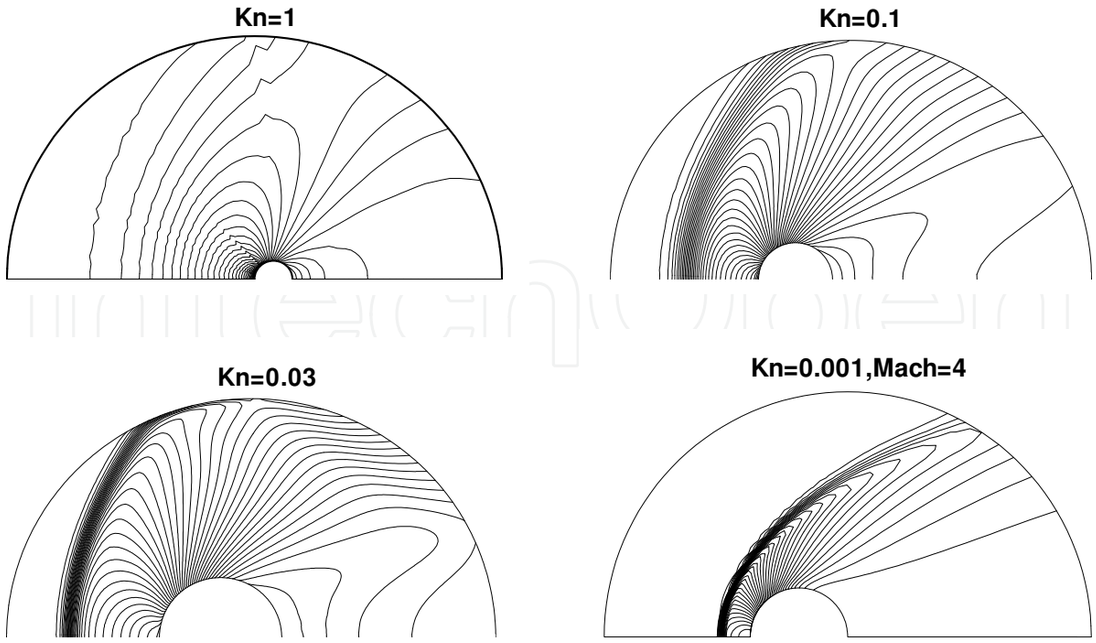

Fig. 13. Pressure contours of cylinder for supersonic flows with various Kn

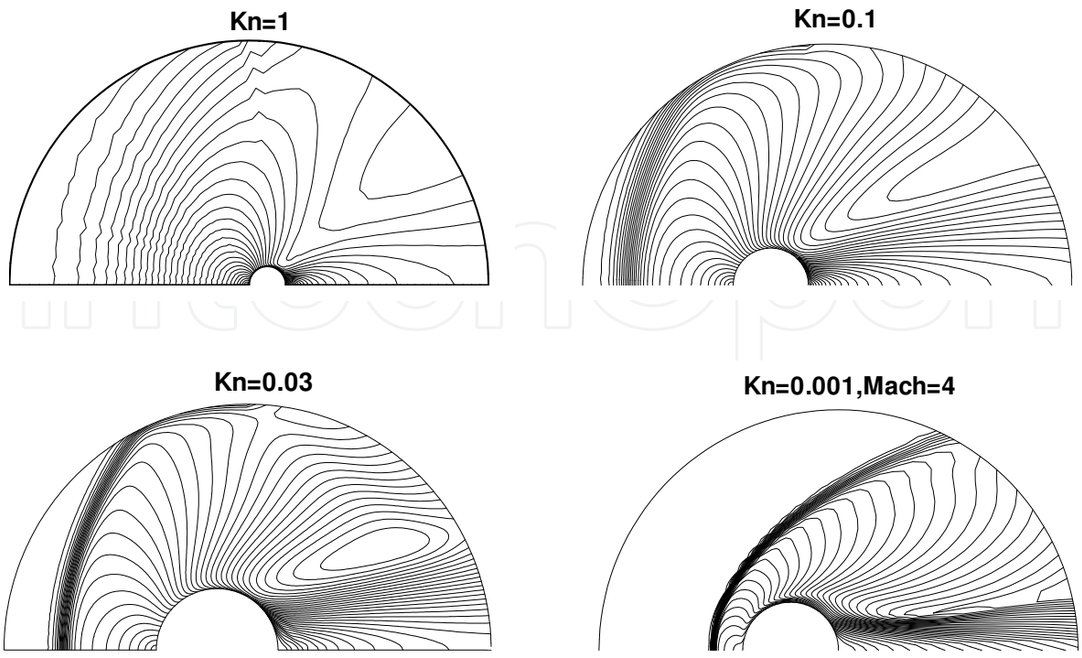

Fig. 14. Mach number contours of cylinder for supersonic flows with various Kn

To try out the computation of the present algorithm to the two-dimensional continuum flow, the case of $Kn = 0.0001$, $M_\infty = 1.8$, $\Pr = 2/3$, $T_w = T_0$ and $\gamma = 5/3$ in the continuum flow regime was set with the 71×51 space cells and the modified Gauss-Hermite quadrature formula with 32×16 discrete points. The computed results of pressure, density, temperature, Mach number contours, and wake flow structures are shown in Fig.15. The flow structures including the front bow shock, the stagnation region, the recompression shock, and the wake region are captured very well. An enlarged view of the recirculation zone past the circular cylinder is scored clearly in Fig.15(e), as is only the feature of the continuum flow.

For comparison purpose, the computed results from Yang & Huang (1995b) using a Navier-Stokes solver (based on a high resolution finite-difference method) are also shown in Fig.16 for the similar flow conditions ($\mathrm{Re}_D = 2996$, $M_\infty = 1.8$). By comparing the results shown in Fig.15 to those shown in Fig.16, it can be found that most of the flow structures are similar. The distribution of the pressure along wall surface for the state of $Kn = 0.0001$ and $M_\infty = 1.8$ is shown in Fig.17 together with the continuum theoretic data from Любимов & Русањов (1970). In Fig.17, the horizontal coordinates denote the angle along wall surface far from the stagnation line between the free-stream direction and the outward direction normal to the wall surface, the vertical coordinates denote the non-dimensional pressure, the symbols (o) indicate the continuum theoretic solutions from Любимов & Русањов (1970), the symbols (●) indicate the computed results. It's shown that the computed results agree with the continuum theoretic data. The foregoing comparisons from Fig.15-17 confirm that the present method is reliable in solving continuum gas flows.

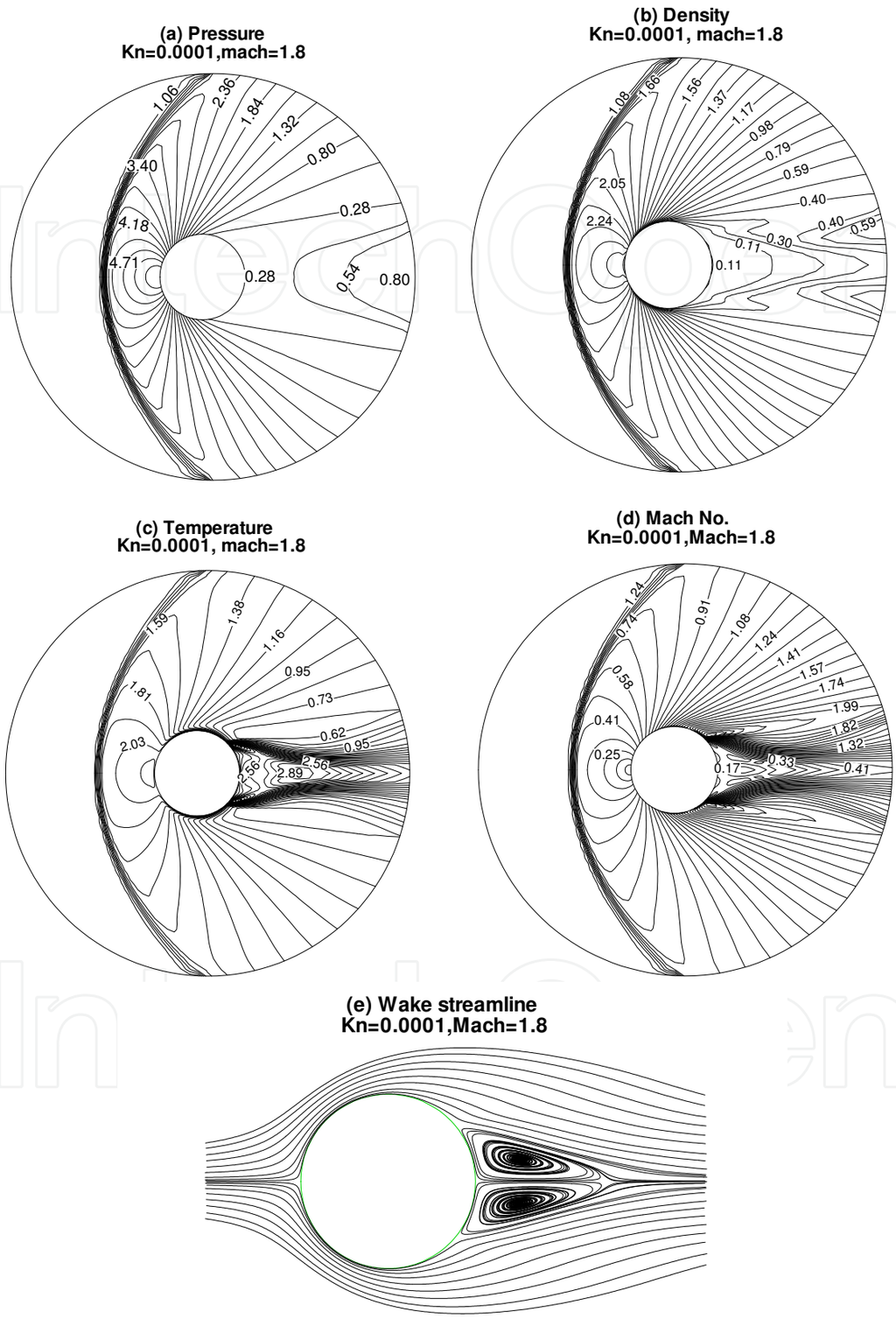

Fig. 15. Computed results of pressure, density, temperature, Mach number and wake streamline for $Kn = 10^{-4}$, $M_\infty = 1.8$.

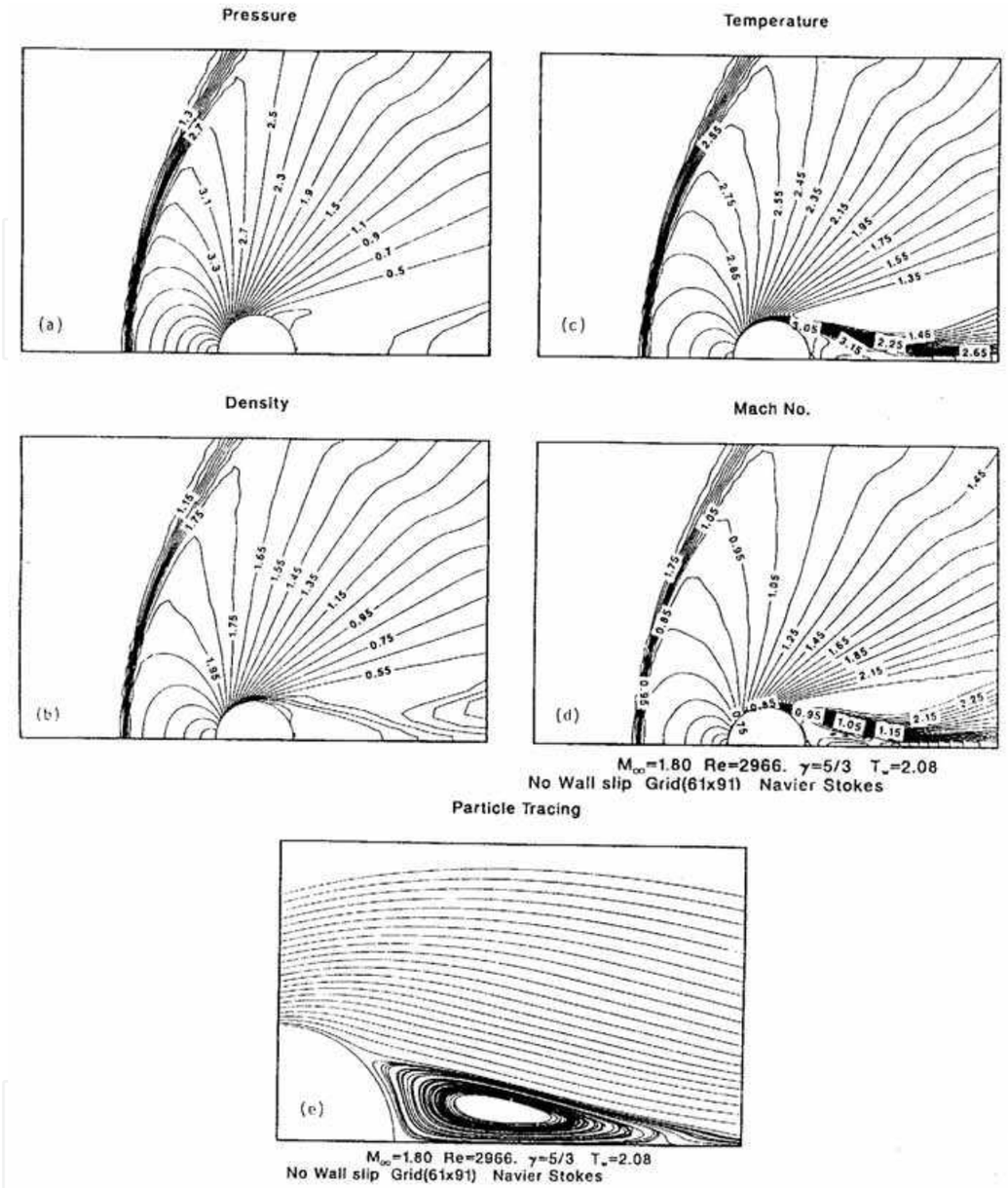

Fig. 16. Continuum Navier-Stokes solutions past cylinder for $M_\infty = 1.8$, $\mathrm{Re}_D = 2966$ from Yang & Hsu (1992).

The stagnation line profiles of density are shown in Fig.18 together with the DSMC results from Vogenitz etc.(1968) for two Knudsen numbers ($Kn = 1$, 0.3) with the states of $M_\infty = 1.8$, $\mathrm{Pr} = 1$, $T_w/T_0 = 1$. Here, the space grid system used is 41×35, and the modified Gauss-Hermite quadrature formula with 32×16 discrete points was employed. In Fig.18, the solid line denotes the computed $Kn = 0.3$ results, the symbols (□) denote the DSMC results of $Kn = 0.3$, the dashed line denotes the computed $Kn = 1$ results, and the symbols (Δ) denote the DSMC results of $Kn = 1$. In general good agreement between the present computations and DSMC solutions can be observed.

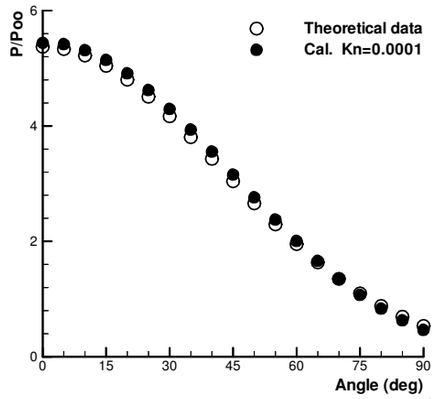

Fig. 17. Pressure distribution along surface.

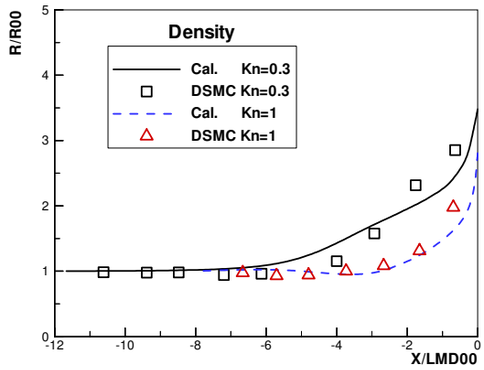

Fig. 18. Stagnation line density profiles

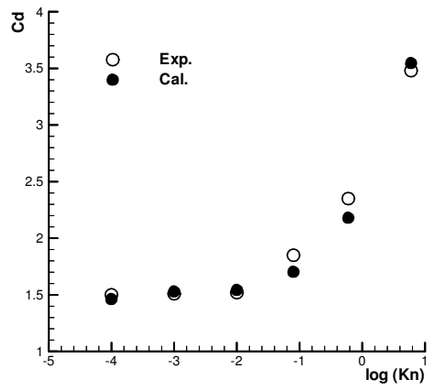

Fig. 19. Drag coefficients of cylinder

In Fig.19, the comparisons between the calculated cylinder drag coefficients and experimental data for argon gas are given for the cases of $M_\infty = 1.96$, $\Pr = 2/3$, $T_w/T_0 = 0.7$, $\gamma = 5/3$, $Kn = 6$, 0.6, 0.08, 0.01, 0.001, and 0.0001. The symbols (o) denote the experimental data from Maslach & Schaaf (1963) and the relevant continuum flow limit solution, and the symbols (●) denote the computed results. It's shown that the computed results agree with the experimental data very well.

8.4 Parallel computation of three-dimensional complex problems covering various flow regimes

It has been made out from the computation of the three-dimensional flows that the present unified algorithm requires to use six-dimensional array to access the discrete velocity distribution functions for every points in the discrete velocity space and physical space so that a great deal of computer memory needs to be occupied in solving three-dimensional flow problems. It is impractical using serial computers at the present time for the present algorithm to run the careful computation of three-dimensional complex problems. The inner concurrent peculiarity of the gas kinetic numerical method makes good opportunities for computing complex flow problems. To test the performance of the parallel program described in Section 6, the speed-up ratio and parallel efficiency are respectively shown in Fig.20 and Fig.21 from 6 to 1024 processors.

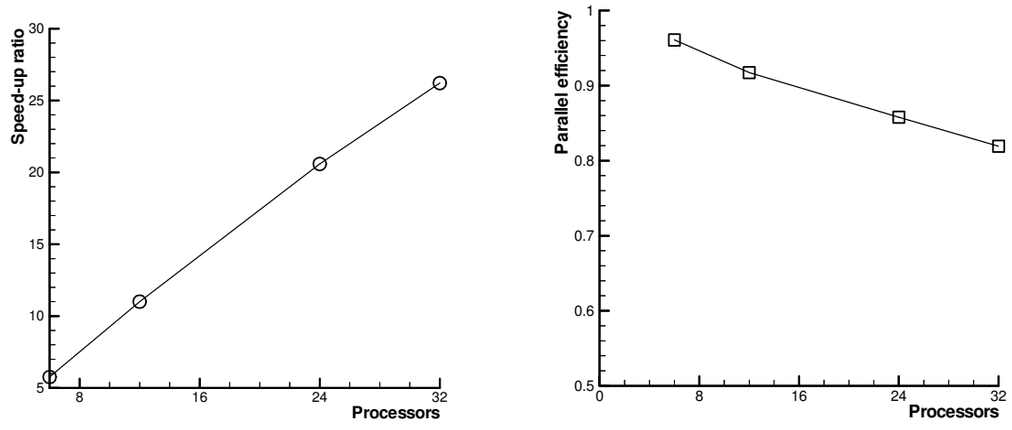

(a) (b)

Fig. 20. (a) Speed-up ratio (b) Parallel efficiency

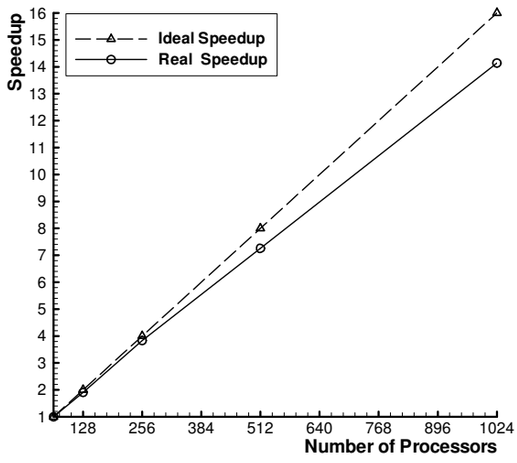

Fig. 21. Parallel speedup ratio based on 64 processors for gas-kinetic parallel algorithm

It can be shown that the unified algorithm is quite suitable for parallel calculations, and the efficiency of concurrent calculations is found rather high.

8.4.1 Three-dimensional sphere flows from rarefied to continuum regime

To investigate the nature of the three-dimensional gas flows, which covers various flow regimes, and to verify the present gas-kinetic numerical models, the basic blunt configuration exemplified by a sphere will be studied and analyzed in detail. A wide range of engineering studies associated with re-entry vehicles are concerned with the aerodynamics of low-density flows in the transitional flow regime between continuum and free-molecule flows. The determination of sphere drag has been for long time a classical problem in aerodynamics. Unfortunately, there are few reliable complete calculations, and careful comparisons between theory and experiment of sphere drag in the transitional flight regime with Reynolds numbers below about 2000. In order to resolve this state of affairs and to gain a comparison with the experimental measurements from Peter & Harry(1962), sphere flows with intermediate Mach numbers for $3.8 < M_\infty < 4.3$ are computed under the cases of ten with the sets of $\Pr = 0.72$, $T_w / T_0 = 1$, $\gamma = 1.4$, $\chi = 0.75$, where the free-stream Knudsen numbers are in the range of $0.006 < Kn_\infty < 0.107$ with the corresponding free-stream Reynolds number of $50 < \mathrm{Re}_\infty < 1000$. To save computer memory with a resource of 32 processors, the space grid points used are only $25 \times 17 \times 21$ with streamwise, circumferential and surface normal directions. The Gauss quadrature formula with the weight function $2/\pi^{1/2}\exp(-x^2)$, described in section 3.2, is employed in the discrete velocity numerical integration method to determine macroscopic flow parameters. Table 1 illustrates the computed results of the drag coefficients of the sphere with the comparison of the experimental data from Peter & Harry(1962).

$d_s(m)$ [a]	0.0191	0.0381	0.0476	0.0381	0.0476	0.0476	0.0572	0.1143	0.1524	0.1523
M_∞ [b]	3.865	3.865	3.863	4.169	4.096	4.322	4.324	4.275	4.229	4.322
Kn_∞ [c]	0.1071	0.0550	0.0447	0.0350	0.0319	0.0203	0.0163	0.0094	0.0079	0.0064
$H(km)$ [d]	76.525	76.732	76.841	73.522	74.466	71.113	70.828	71.913	72.765	71.180
$C_{D,Exp}$ [e]	1.713	1.502	1.452	1.337	1.336	1.275	1.229	1.227	1.206	1.177
$C_{D,Cal}$ [f]	1.743	1.491	1.457	1.411	1.389	1.279	1.255	1.233	1.212	1.211
$Error(\%)$ [g]	1.75%	0.73%	0.34%	5.53%	3.97%	0.31%	2.12%	0.49%	0.50%	2.89%

a Diameter of sphere in meter. b Mach number of the freestream. c Knudsen number of the freestream. d Flying altitude in kilometer corresponding to d_s and Kn_∞. e Drag coefficient from the experiment in Peter & Harry (1962). f Drag coefficient from the present computation. g The relative error.

Table 1. Drag coefficients of sphere for $3.8 < M_\infty < 4.3$, $0.006 < Kn_\infty < 0.107$ in the transition flow regime

Each column, from the second to the eleventh, respectively refers to the simulation of ten cases: the parameters including the diameter d_s of the sphere, the Mach number M_∞ and Knudsen number Kn_∞ of the freestream in the front three rows of that column are given from the experiment reference and are used as input to the simulation code, and then the values below are output. To provide physical insight concerning the flying states of transitional flows, the flying altitude $H(km)$ of the sphere relative to the given free-stream Knudsen number Kn_∞ and the diameter d_s of the sphere are educed with the range of

$70km < H < 77km$ and also shown in the fourth row of Tab.1. It is seen from Tab.1 that the computed drag coefficients, in the sixth row, are in excellent agreement with the experimental data indicated in the fifth row with all of Knudsen numbers from $Kn_\infty = 0.1071$ to $Kn_\infty = 0.0064$. The relative differences denoted in the seventh row are of the order of 0.31%~5.53%, which indicates that the present algorithm has good capability in computing the aerodynamics of the rarefied transitional flow even though the coarse spatial mesh system is used. To analyze and compare the flow structures past the sphere with the DSMC solutions from Vogenitz etc.(1968), the flow state of $Kn_\infty = 0.03$, $M_\infty = 3.83$, $\Pr = 2/3$, $T_w / T_0 = 1$, $\gamma = 5/3$, $\chi = 0.75$ from the near-continuum transitional regime is studied. Fig.22 shows the variation of temperature and flow velocity on the stagnation line in front of the body, where the vertical ordinate of $(T - T_{oo})/(T_o - T_{oo})$ and U / V_{oo} respectively denote the non-dimensionalized temperature $(T - T_\infty)/(T_o - T_\infty)$ and velocity $\left|\vec{U}\right| / V_\infty$ distribution, and the abscissa denotes the non-dimensionalized position from the stagnation point in the direction of the freestream.

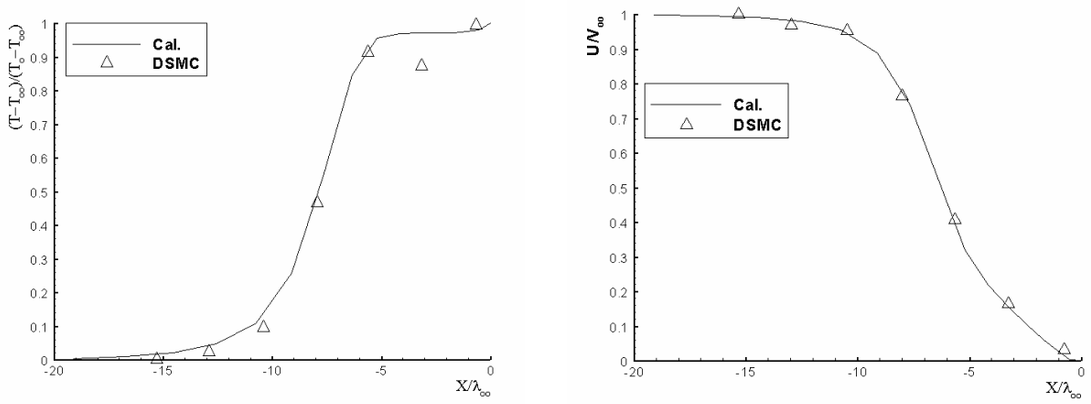

(a) Temperature (b) flow velocity

Fig. 22. Stagnation-line profiles for a sphere with $Kn_\infty = 0.03$, $M_\infty = 3.83$, where X / λ_∞ is the distance from the stagnation point of body surface. Solid line, present computations; delta, DSMC results.

As shown in Fig.22, the computed profiles agree with the DSMC results, however, some difference appears in the temperature profiles from Fig.22(a), as seems to result from the considerable statistical scatter of the DSMC results. For the comparison of the drag coefficient of the above-mentioned sphere, the present computed value of $C_{D,Cal} = 1.3749$ is in good agreement with the DSMC result of $C_{D,DSMC} = 1.4122$ with the relative deviation of 2.64%, even though the present computation is performed in quite a coarse spatial mesh system of $25 \times 19 \times 27$, as indicates that the present algorithm isn't sensitive to spatial grid division with strong and stable capability of computing convergence.

Rarefied hypersonic flows about bodies are of greatest practical interest. The hypersonic flows in the near-continuum transitional regime are difficult to treat either experimentally or theoretically over an altitude range of $40km \sim 90km$. To illustrate the capability of the present gas-kinetic numerical method for hypersonic Mach number flows and to apperceive the physical nature of hypersonic transition flows, eight cases of hypersonic flows past sphere are computed with the sets of $\Pr = 0.72$, $T_w = 300k$, $\gamma = 1.4$, $\chi = 0.75$ with different

Reynolds numbers Re_2 behind the wave and Mach numbers of $M_\infty = 8.65$, 8.68, 10.39, 13 from the low-density wind tunnel test conditions of Koppenwallner & Legge (1985). Table 2 summarizes the computing parameters of the above states, where each column from the second to the ninth respectively refers to the flow state of eight cases, parameters, including the diameter d_s of the sphere, the Mach number M_∞ of the freestream and the Reynolds number Re_2 behind the normal wave in the front three rows of that column, are given from the experiment reference and are also used as input to the simulation code. The other values including the free-stream Knudsen numbers (Kn_∞), Reynolds numbers (Re_∞) and the relevant flight altitudes $H(km)$ are obtained from the computation.

$d_s(m)$ [a]	0.04	0.04	0.04	0.005	0.003	0.001	0.001	0.001
M_∞ [b]	13.00	13.00	13.00	10.39	8.68	8.65	8.65	8.65
Re_2 [c]	271.53	191.61	113.60	23.62	10.093	3.3996	0.9926	0.1985
Kn_∞ [d]	0.0050	0.0071	0.0119	0.0640	0.1616	0.4827	1.6532	8.2659
Re_∞ [e]	3943.13	2782.54	1649.69	245.32	131.11	27.07	7.90	1.58
$H(km)$ [f]	58.07	60.96	65.44	62.01	61.45	65.55	75.07	84.79

a Diameter of sphere in meters. b Mach number of the freestream. c Reynolds number behind the normal shock. d Knudsen number of the freestream related to M_∞ and Re_2. e Reynolds number of the freestream. f Flying altitude in kilometer related to d_s and Kn_∞.

Table 2. Computed states of hypersonic flows of $M_\infty = 8.65$, 8.68, 10.39, and 13 past sphere for $0.005 \le Kn_\infty \le 8.266$, $58km < H < 85km$, $1.5 < \mathrm{Re}_\infty < 3950$

It can be shown from Tab.2 that the flying altitude corresponding to the considered eight cases is in the range of $58km < H < 85km$ and the free-stream Knudsen number is in the wide range of $0.005 < Kn_\infty < 8.266$ with $1.5 < \mathrm{Re}_\infty < 3950$ relative to the small characteristic length of sphere diameter. The computed results of the drag coefficients as a function of the free-stream Knudsen numbers are shown in Fig.23 together with the early experimental data, see Koppenwallner & Legge (1985). In this case, the abscissa (Kn) denotes the logarithm values of Kn_∞, and the vertical ordinate denotes the drag coefficient (C_D) of sphere. In general, the agreement between the present computations and the experiments can be observed well.

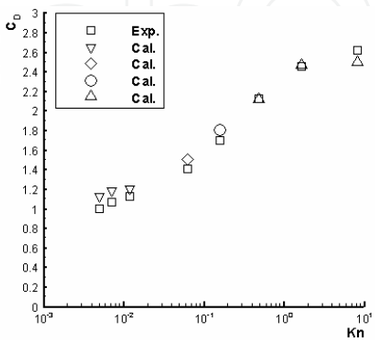

Fig. 23. Drag coefficients for hypersonic flow past a sphere. Square (□) represents experimental data in Koppenwallner & Legge (1985); other symbols denote the present computed results, where gradient (∇) corresponds to $M_\infty = 13$, diamond (◊) corresponds to $M_\infty = 10.39$, circle (O) corresponds to $M_\infty = 8.68$, delta (Δ) corresponds to $M_\infty = 8.65$.

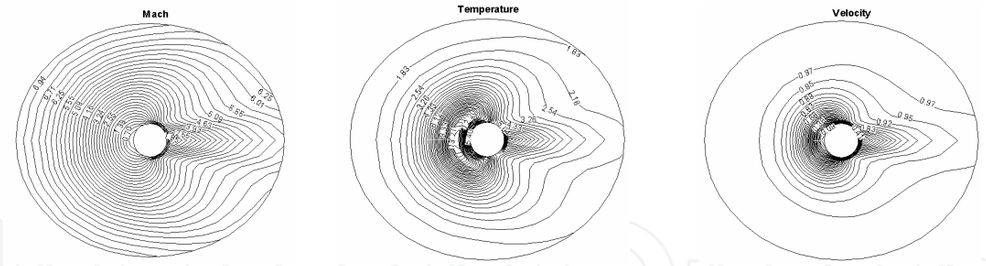

(a) $Kn_\infty = 1.6532$, $M_\infty = 8.65$

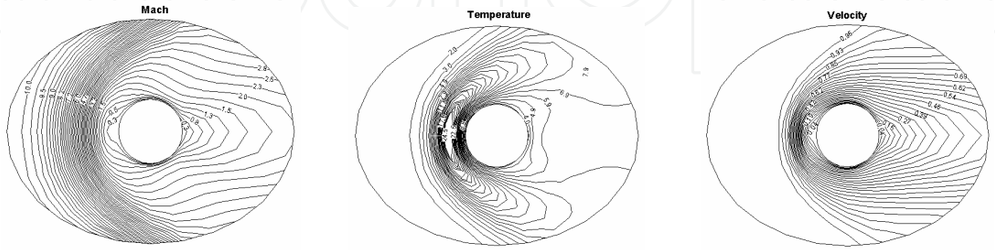

(b) $Kn_\infty = 0.064$, $M_\infty = 10.39$

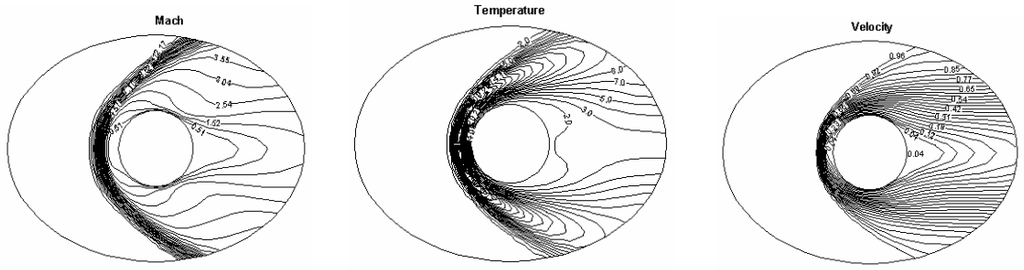

(c) $Kn_\infty = 0.0071$, $M_\infty = 13$

Fig. 24. Mach, temperature and flow velocity contours of hypersonic flows past sphere.

Fig.24 shows the flow field contours of Mach number, temperature and flow velocity in the symmetrical plane around the sphere corresponding to the aforementioned flow states of (a) $Kn_\infty = 1.6532$, $M_\infty = 8.65$, (b) $Kn_\infty = 0.064$, $M_\infty = 10.39$ and (c) $Kn_\infty = 0.0071$, $M_\infty = 13$, where the numeral on the contours including all of figures denotes the normalized magnitude of related flow parameters. It can be indicated from Fig.24 that the flow decelerates gradually as it approaches the body. The disturbed region of flow becomes wider for the full rarefied flow with higher Knudsen number of $Kn_\infty = 1.6532$. The disturbed zone of the blurry shock wave appears in front of the body for the rarefied transitional flow of $Kn_\infty = 0.064$, and in the end, a thick and explicit bow shock wave is formed so that the flow field is clearly divided into the undisturbed gas and the disturbed one in the hypersonic near-continuum flow of $Kn_\infty = 0.0071$, $M_\infty = 13$. Furthermore, it exists a zone of high temperature in the contours of temperature due to the cooled body with low surface temperature, the hypersonic flow around the body passes by the zenith with the supersonic expansion, and there does not form any recompression phenomena in the back of the body.

To numerically analyze the flow features and physical nature, from various flow regimes, and to test the reliability of the present gas-kinetic algorithm in solving three-dimensional flow problems from rarefied transition to continuum regime, four cases of the $M_\infty = 3$ flow past sphere with $Kn_\infty = 1$, 0.1, 0.01 and 0.0001, $\Pr = 2/3$, $T_w / T_0 = 1$, $\chi = 0.75$ are investigated by the HPF parallel computation. In this instance, the modified Gauss-type quadrature method for the discrete velocity space is employed with the $41 \times 21 \times 35$ spatial cells in the physical space. It can be shown from the flow velocity contours, in Fig.25, that for the fully rarefied flow related to $Kn_\infty = 1$, the disturbed region of flow is quite large and the flow decelerates gradually clinging to the body surface as it approaches the sphere.

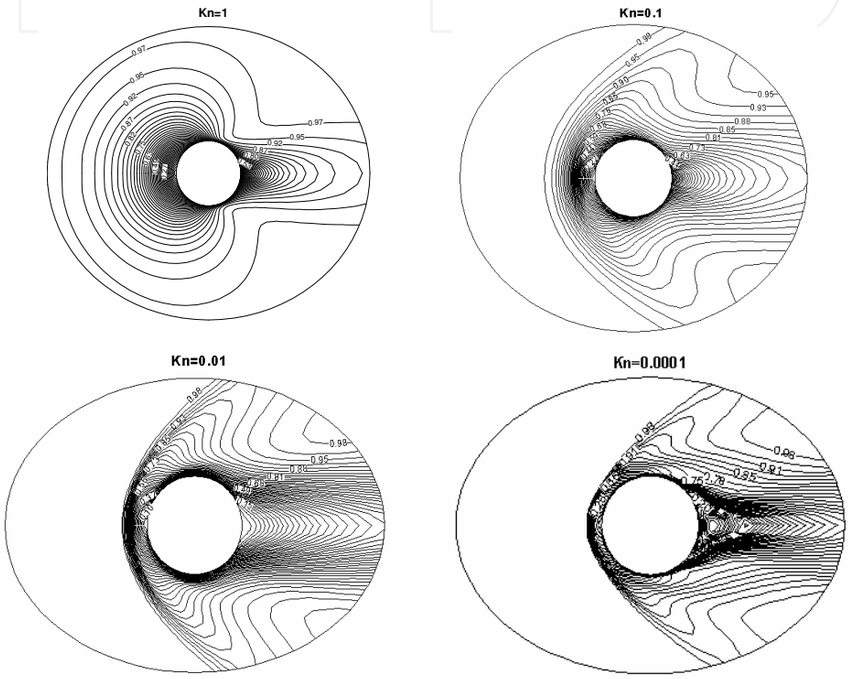

Fig. 25. Flow velocity contours in the symmetrical plane around sphere for $Kn_\infty = 1$, 0.1, 0.01 and 0.0001 with $M_\infty = 3$.

As the Knudsen number decreases from $Kn_\infty = 1$ to $Kn_\infty = 0.0001$, the disturbed region of flow becomes smaller and smaller near the body, and the strong disturbance, the dim bow shock and the recompression phenomena of the flow, appear in the rarefied transition flows related to $Kn_\infty = 0.1$ and $Kn_\infty = 0.01$. For the supersonic continuum flow of $Kn_\infty = 0.0001$, the flow structures including the thin front bow shock, the stagnation region, the accompanied weak shock wave beyond the top of sphere, the recompressing shock wave formed by the turning of the flow and the wake region are captured well. Further more, the front bow shock wave is closer to the body when the flow approaches the continuum flow from the near-continuum transition flow by diminishing the Knudsen number from $Kn_\infty = 0.1$ to $Kn_\infty = 0.0001$. The streamline structures in the symmetrical plane around sphere for the cases of $Kn_\infty = 0.1$, $Kn_\infty = 0.01$ and $Kn_\infty = 0.0001$ are shown in Fig.26, where the arrowhead on the streamline denotes the flow direction, and the symbol (Kn) in all of figures denotes the free-stream Knudsen number (Kn_∞).

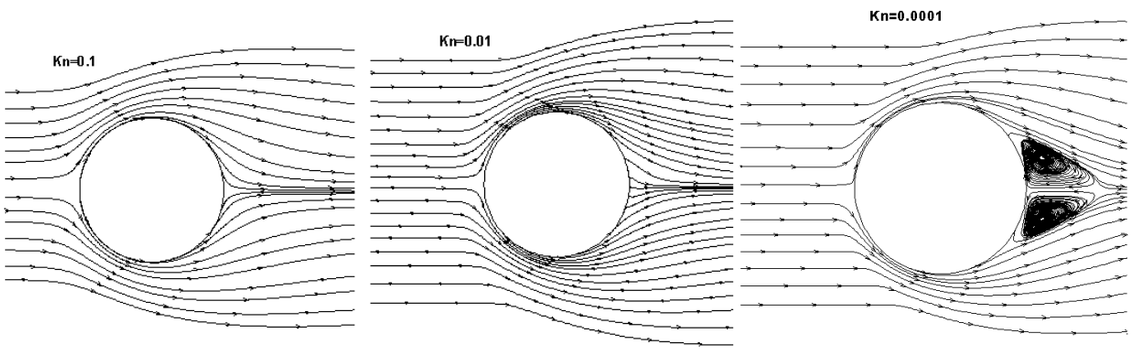

Fig. 26. Streamlines in the symmetrical plane around sphere for $Kn_\infty = 0.1$, 0.01 and 0.0001 with $M_\infty = 3$

It can be seen that for rarefied transitional flows of $Kn_\infty = 0.1$ and $Kn_\infty = 0.01$, the flow is attached to the sphere surface with strong wall slip effect of flow velocity, and there is no evidence of flow separation in the wake, as is expected for this two rarefied flow conditions of $\mathrm{Re}_\infty = 43.67$ and $\mathrm{Re}_\infty = 436.67$. However, for the case of $Kn_\infty = 0.0001$, the boundary layer flow separation behind the sphere is clearly visible and the separated vortices exist in the wake with well defined recirculation zones as the feature of the continuum flow. The flow details of the boundary layer separation, the separated vortex, and the near wake will be stable for this flow with the Reynolds number of $\mathrm{Re}_\infty = 43666.96$. Fig.27 qualitatively reveals the variation of collision frequency with different position points in the interior of the flow field for various flow regimes from $Kn_\infty = 1$ to $Kn_\infty = 0.0001$. It can be illustrated that the collision frequency is entirely different with variation of spatial position in the same flow field around the body. For the completely rarefied flow of $Kn_\infty = 1$, $M_\infty = 3$, the intermolecular collisions are quite rare, the collision frequency just varies from a maximum of about 4.92 near the stagnation point to the minimum value of 10^{-3} near the back-end of the body in the wake region. However, in the rarefied transition flows of $Kn_\infty = 0.1$ and $Kn_\infty = 0.01$ or continuum flow of $Kn_\infty = 0.0001$, the gas becomes more and more dense, the collision frequency rapidly increases and the strong disturbance and bow shock wave appears. Particularly for the case of $Kn_\infty = 0.0001$, $M_\infty = 3$, the collision frequency varies from a maximum of about 71345.2 near the stagnation point to a minimum value of less than 630 in the wake. Fig.28 presents the stagnation line profiles of pressure for the cases of $Kn_\infty = 0.1$, $Kn_\infty = 0.01$ and $Kn_\infty = 0.0001$, respectively.

For the supersonic rarefied flow of $Kn_\infty = 0.1$, $M_\infty = 3$, the pressure rises smoothly and gradually and goes up to the maximum value at the sphere stagnation point as the flow approaches the sphere, which forms a quite wide region of flow disturbance. However, for the near-continuum transition flow with a low Knudsen number of $Kn_\infty = 0.01$, the region of pressure disturbances almost cuts down to half of that for the case of $Kn_\infty = 0.1$, and there exists the faint shock wave in the stagnation-line profiles. For the supersonic continuum flow of $Kn_\infty = 0.0001$, $M_\infty = 3$, the sharp variation of pressure only occurs in the very narrow disturbed domain so much as half of that in the case of $Kn_\infty = 0.01$, and a thin and clear shock wave lies in the stagnation-line near the forepart of the body. Figs.25-28 qualitatively reveal the evolving process and physical phenomena of the flows around the body from the highly rarefied to continuum flow while the Knudsen number diminishes from $Kn_\infty = 1$ to $Kn_\infty = 0.0001$.

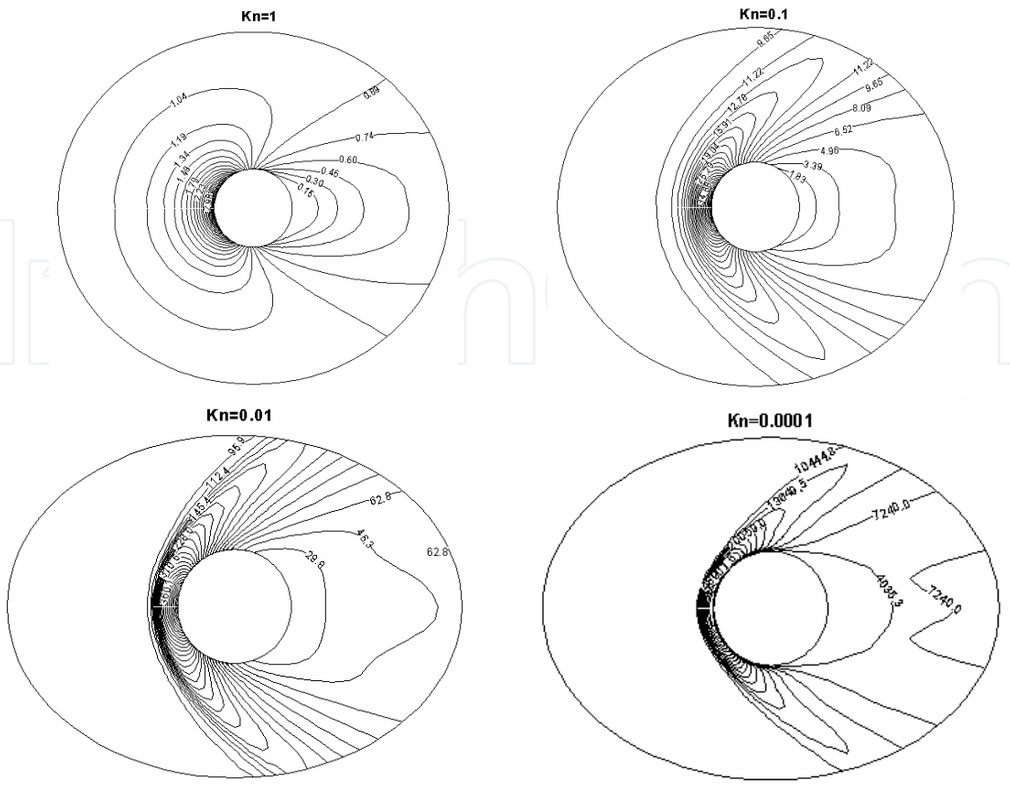

Fig. 27. Variation of collision frequency in the symmetrical plane around sphere for $Kn_\infty = 1$, 0.1, 0.01 and 0.0001 with $M_\infty = 3$.

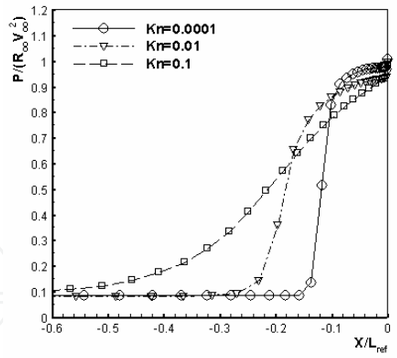

Fig. 28. Stagnation-line pressure profiles of a sphere for $Kn_\infty = 0.1$, 0.01 and 0.0001 with $M_\infty = 3$, where abscissa (X / L_{ref}) is the normalized distance from body surface based on the diameter of sphere, and coordinate ($P / (R_{oo} V_{oo}^2)$ denotes the normalized pressure ($p / (\rho_\infty V_\infty^2)$).

Since the present gas-kinetic algorithm explicitly evaluates the time evolution of the molecular velocity distribution function to update all the macroscopic flow variables, it is different from any other numerical approach where the macroscopic fluid equations are discretized directly, the slip boundary condition can be naturally comprised and satisfied according to the interaction model between the gas and the solid surface. To explore the

wall slip phenomena from various flow regimes and flow details along the body surface, Fig.29 illustrates the normalized tangent velocity (V_t/V_∞), that is so-called wall slip velocity, along the sphere surface in the cases of $Kn_\infty = 0.1$, 0.01 and 0.0001 .

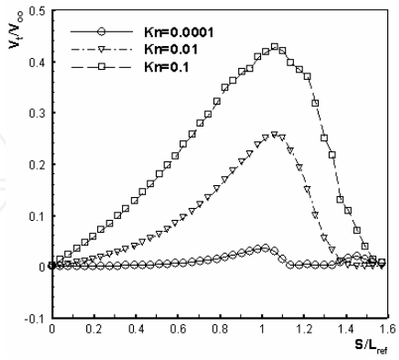

Fig. 29. Slip velocity along the tangent direction of sphere surface for $Kn_\infty = 0.1$, 0.01 and 0.0001 with $M_\infty = 3$, where abscissa (S / L_{ref}) is the normalized surface distance from the stagnation point based on the diameter of sphere, and coordinate (V_t / V_{oo}) denotes the normalized tangent velocity V_t / V_∞ .

For the continuum flow with the very low Knudsen number of $Kn_\infty = 0.0001$, the tangent velocity along the body surface is quite small particularly near the region of the stagnation point so that it can be neglected, which is consistent with the assumption of no slip velocity of macroscopic continuum fluid dynamics. However, even though for the case of $Kn_\infty = 0.0001$ and $M_\infty = 3$, the slip velocity still gradually goes up to the maximum value of about 0.0428 in the region far from the stagnation point, especially beyond the top of the sphere. As the free-stream Knudsen number increases along with augmentation of the effect of gas rarefaction, the magnitude of slip velocity increases rapidly. For the near-continuum flow of $Kn_\infty = 0.01$ and the rarefied transitional flow of $Kn_\infty = 0.1$, on almost all of the body surface exists wall slip phenomena except the front and back stagnation point, particularly for the case of $Kn_\infty = 0.1$, the maximum value of wall slip velocity almost reaches to half of the free-stream velocity, that is about $(V_t/V_\infty)_{\max} = 0.4296$.

8.4.2 Hypersonic flow problems past spacecraft shape

In this subsection, we apply the gas-kinetic algorithm to study three-dimensional complex flows past the spacecraft shape with various Knudsen numbers and Mach numbers. Figures 30 and 31 respectively present the computed results of Mach number and pressure contours for the two cases of $Kn_\infty = 0.5$ and $Kn_\infty = 0.01$ with $M_\infty = 5$, $\alpha = 20°$, $\Pr = 0.72$, $T_w / T_0 = 1$, $\gamma = 1.4$. It can be shown that for the near-continuum flow of $Kn_\infty = 0.01$, the flow structures including the front bow shock, stagnation region and recompression shock are well captured, however, for the highly rarefied flow of $Kn_\infty = 0.5$, there exists the wide domain of flow disturbance around the body with no shock wave and recompression phenomena in the flow field. Figs.30 and 31 qualitatively reveal that the gas flow gradually approaches from highly rarefied flow to near-continuum flow while the Knudsen number diminishes from $Kn_\infty = 0.5$ to $Kn_\infty = 0.01$.

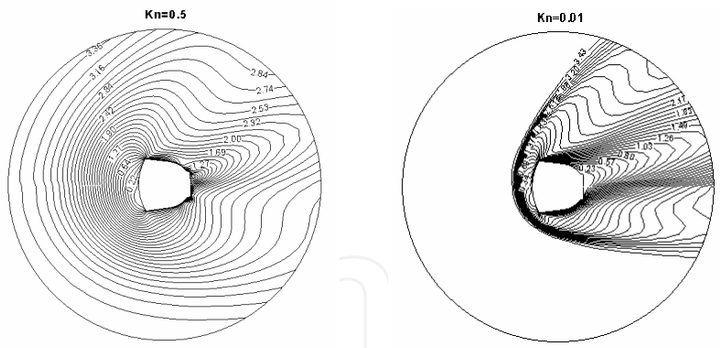

Fig. 30. Mach number contours in the symmetrical plane past spacecraft shape for $Kn_\infty = 0.5$ and $Kn_\infty = 0.01$ with $M_\infty = 5$ and $\alpha = 20°$.

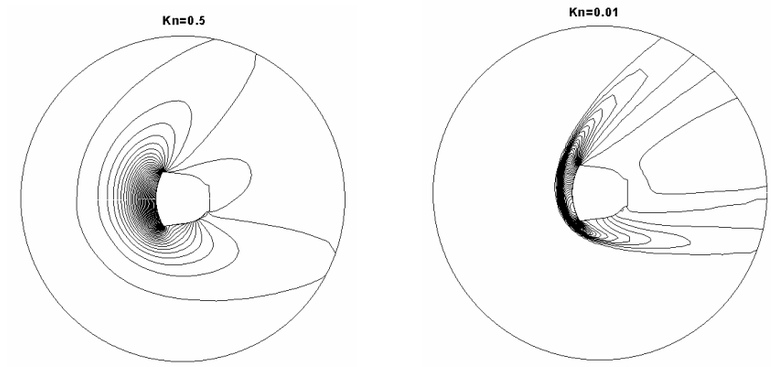

Fig. 31. Pressure contours in the symmetrical plane past spacecraft shape for $Kn_\infty = 0.5$ and $Kn_\infty = 0.01$ with $M_\infty = 5$ and $\alpha = 20°$.

To reveal the variation of stagnation line profiles from various flow regimes, Fig.32 shows the flow velocity distribution past the spacecraft shape along with the stagnation line for the full rarefied flow of $Kn_\infty = 5$, $M_\infty = 4$ and the near-continuum flow of $Kn_\infty = 0.01$, $M_\infty = 4$.

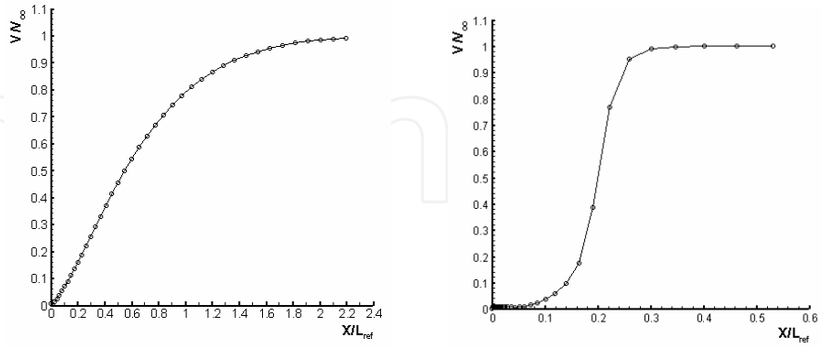

(a) $Kn_\infty = 5$ (b) $Kn_\infty = 0.01$

Fig. 32. Stagnation line velocity profiles from different flow regimes for $Kn_\infty = 5$ and $Kn_\infty = 0.01$ with $M_\infty = 4$, where abscissa (X / L_{ref}) is the normalized distance from the stagnation point of the body, and coordinates (V / V_{oo}) denote the normalized flow velocity $\left|\vec{U}\right| / V_\infty$.

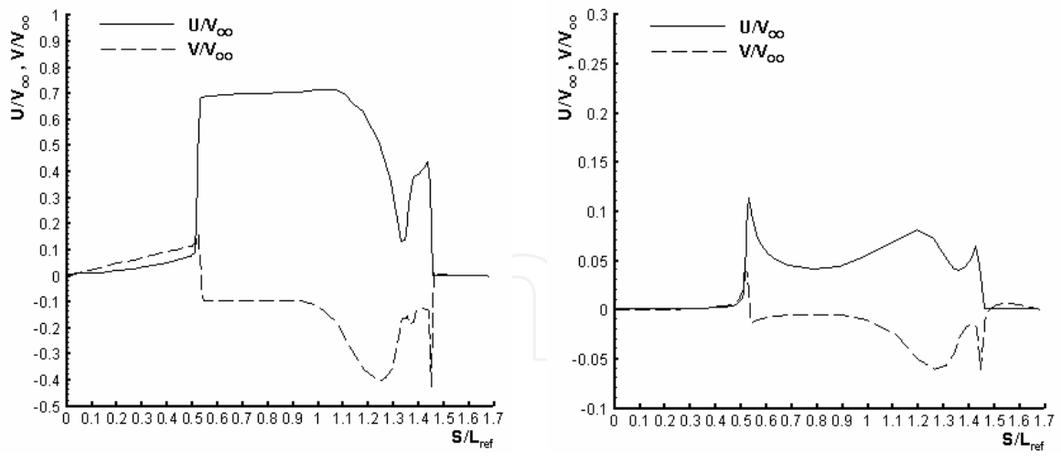

(a) $Kn_\infty = 5$ (b) $Kn_\infty = 0.01$

Fig. 33. Axial and lateral flow velocity distribution along the body surface in the symmetric plane around the spacecraft shape for $Kn_\infty = 5$ and $Kn_\infty = 0.01$ with $M_\infty = 4$ and $\alpha = 0°$, where abscissa (S / L_{ref}) is the normalized surface distance from the forefront point of the body, and coordinates ($U / V_{oo}, V / V_{oo}$) denote the normalized velocity U / V_∞ and V / V_∞ in axial and lateral direction, respectively.

In the rarefied flow regime, the flow velocity smoothly and gradually increases from the zero at the stagnation point to the free-stream value near the undisturbed outer boundary for the case of $Kn_\infty = 5$, $M_\infty = 4$, which undergos a wider region of disturbed flow up to two more times of the characteristic length of the body. However, in the near-continuum transitional flow regime, the flow velocity almostly approximates to zero in the vicinity of the stagnation point, and at some distance far from the stagnation point, the flow velocity sharply goes up with distinctly jumping phenomena, then approaches the free-stream value corresponding to the near-continuum flow of $Kn_\infty = 0.01$, $M_\infty = 4$. It is indicated from Fig.32(b) that the flow phenomna of the front bow shock wave is in a very narrow disturbed domain as much as one fifth of that corresponding to the full rarefied flow of $Kn_\infty = 5$, $M_\infty = 4$. Fig.33 shows the normalized wall velocity components U/V_∞ and V/V_∞ in the symmetrical plane along the body surface from the stagnation point related to the two cases of $Kn_\infty = 5$ and $Kn_\infty = 0.01$ with $M_\infty = 4$, $\alpha = 0°$. It can be revealed that the wall velocity diminishes down to zero in the vicinity of the front and back stagnation point. However, a distinct wall slip velocity exists far from the stagnation point both for the high rarefied flow of $Kn_\infty = 5$ and for the near-continuum flow of $Kn_\infty = 0.01$. While the free-stream Knudsen number increases from $Kn_\infty = 0.01$ to $Kn_\infty = 5$, the effect of gas rarefaction is greatly enhanced, which induces that the wall slip velocity increases rapidly so that the maximum value of the wall slip velocity is more than half of the free stream velocity for the case of $Kn_\infty = 5$, $M_\infty = 4$. To reveal the varying characteristic of surface heat flux covering various flow regimes, Figs.34 and 35 respectively show the distribution of heat flux $q/(\rho_\infty a_\infty^3)$ along the streamwise surface of the spacecraft for two cases of $Kn_\infty = 5$, $M_\infty = 4$, $\alpha = 0°$ and $Kn_\infty = 0.001$, $M_\infty = 4$, $\alpha = 20°$, where the horizontal coordinates denote the surface distance S/L_{ref} from the front end point of the body along stream direction.

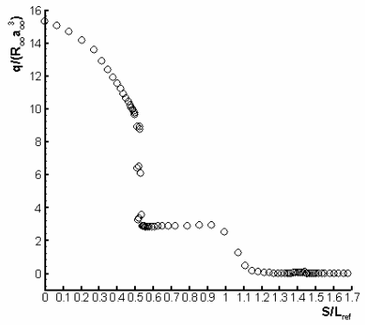

Fig. 34. Heat flux distribution along the body surface past spacecraft shape for $Kn_\infty = 5$, $M_\infty = 4$ and $\alpha = 0°$, where abscissa (S / L_{ref}) is the normalized surface distance from the forefront point of the body, and coordinate $q / (R_{oo} a_{oo}^3)$ denotes the magnitude of normalized heat flux $q / (\rho_\infty a_\infty^3)$.

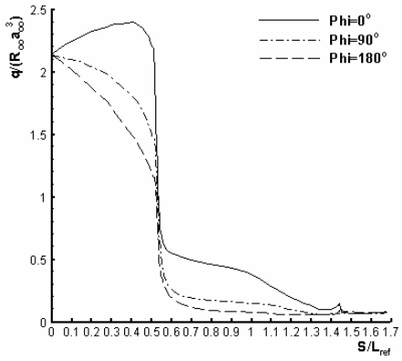

Fig. 35. Heat flux distribution along the body surface in different meridian planes of $\varphi = 0°, 90°, 180°$ past spacecraft shape for $Kn_\infty = 0.001$, $M_\infty = 4$ and $\alpha = 20°$.

It can be shown from Fig.34 corresponding to the full rarefied flow of $Kn_\infty = 5$, $M_\infty = 4$, with $\alpha = 0°$ that the maximum value of surface heat flux appears at the front end point of the body, the surface heat flux descends gradually along with the variation of surface curvature, and the surface heat flux goes sharply down across the top of the body, then holds the line on the whole in course of the surface of the inversion cone, ultimately drops down to zero in the leeward region of the spacecraft, which reflects the peculiarity of attaching wall flow in the high rarefied flow regime. Fig.35 shows the distribution of the surface heat flux along with the three symmetrical meridian planes of $\phi = 0°$, $90°$, $180°$ related to the case of supersonic continuum flow of $Kn_\infty = 0.001$, $M_\infty = 4$, $\alpha = 20°$. For the windward plane of $\phi = 0°$, the surface heat flux gradually goes up and reaches the maximum value at the top of the body; however for the cross-stream plane of $\phi = 90°$ and the leeward plane of $\phi = 180°$ the maximum heat flux arises at the front end point of the body. In the region of the afterbody across the top of the body, the surface heat flux goes sharply down owing to the rapid expansion of the flow so that the heat flux turns to the minimum in the back end of the body. It can be validated from Figs.34 and 35 that the surface heat flux for the full rarefied flow of $Kn_\infty = 5$, $M_\infty = 4$ is six times as much as that for the near-continuum flow of $Kn_\infty = 0.001$, $M_\infty = 4$.

To numerically analyze and compare the variation of flow pattern, from rarefied to continuum regime around three-dimensional complex bodies, Fig.36 shows the vector streamline structures around the spacecraft shape for the three cases of $Kn = 5$, $Kn = 0.01$ and $Kn_\infty = 0.001$ with $M_\infty = 4$ under different angles of attack $\alpha = 0°$ and $\alpha = 20°$.

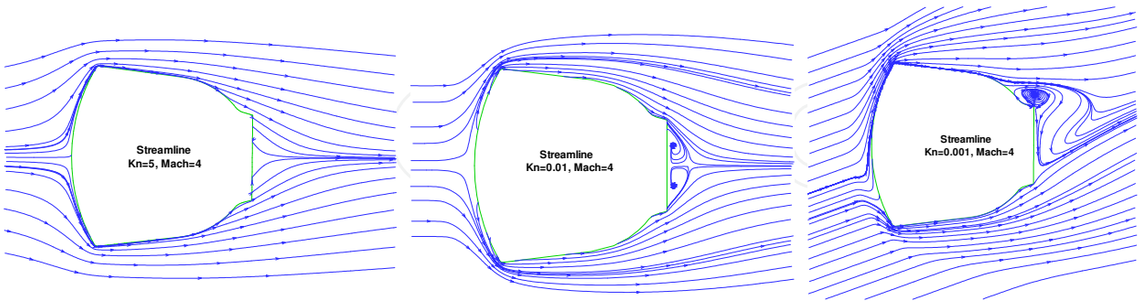

(a) $Kn_\infty = 5, \alpha = 0°$ (b) $Kn_\infty = 0.01, \alpha = 0°$ (c) $Kn_\infty = 0.001, \alpha = 20°$

Fig. 36. Flow structures in the symmetric plane around spacecraft shape for $Kn_\infty = 5$, $Kn_\infty = 0.01$ and $Kn_\infty = 0.001$ with $M_\infty = 4$, $\alpha = 0°$ and $20°$.

It can be seen that for high rarefied flow of $Kn = 5$, it is completely attached to the surface with strong wall slip effect and there is no evidence of flow separation in the back of the body. However, in the near-continuum transition flow with low Knudsen number of $Kn = 0.01$, the flow separation and vortex wake structures emerge from the rearward region of the body. For the case of supersonic continuum flow with $Kn_\infty = 0.001$, $M_\infty = 4$, the boundary layer flow separation in the region of the afterbody is clearly visible and the separated vortex exists in the wake with a well defined recirculation zone, as it is only a particular feature of continuum gas flow. The above computations nicely tally with the theoretical predictions and affirm the flow phenomena and characteristic past the complex shape.

To solve the problem of the trim angle of attack of the reentry flight, we compute and study the flying states of hypersonic Mach number flow past the spacecraft shape for the flying case of $Kn_\infty = 0.0063$, $M_\infty = 15.587$, $\mathrm{Re}_\infty = 3729.15$ and $T_w / T_0 = 0.5435$. Fig.37(a) illustrates the Mach number contours in the symmetrical plane past the body with the flying angle of attack of $\alpha = 26°$. It can be observed from Fig.37(a) and the above-mentioned Fig.34, Fig.35 and Fig.30 that no recompression shock exists in the hypersonic flows around the body, which exhibits the flow characteristic remarkably different from supersonic flows, and that the hypersonic flow generally expands supersonically beyond the top of the body and remains supersonic in most of the wake region. Fig.37(b) presents the pitching moment coefficient C_{mg} relative to the centre of mass as a function of angle of attack α for the relevant flight altitude of $H = 88.34km$, where the symbols of circle (O) denote the present computed results for $\alpha = 15°$, $18°$, $20°$, $22°$, $26°$, $30°$ and the delta (Δ) corresponds to the experimental data (Dai,Yang & Li 2004) from low-density hypervelocity wind tunnel. It can be shown from the comparison that the present computations of C_{mg} are in good agreement with the experiments, where the computed trim angle of attack is $\alpha_{Cal} = 25.06°$ and the experimental measurement is about $\alpha_{Exp} = 25.39°$.

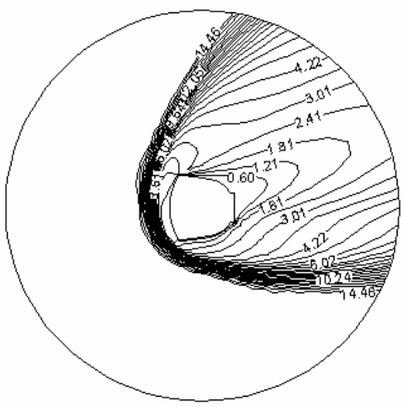

(a) Mach number contours with $\alpha = 26°$

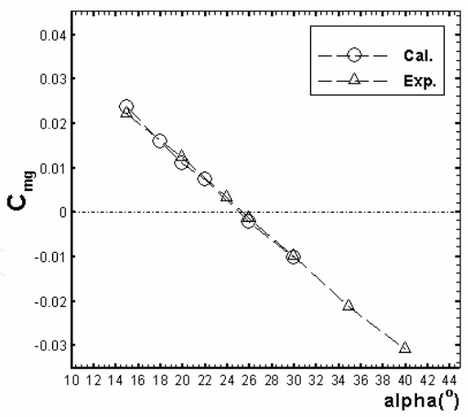

(b) Pitching moment coefficient C_{mg} vs $\alpha(°)$

Fig. 37. Hypersonic flow past spacecraft shape for $Kn_\infty = 0.0063$, $M_\infty = 15.587$, $\mathrm{Re}_\infty = 3729.15$.

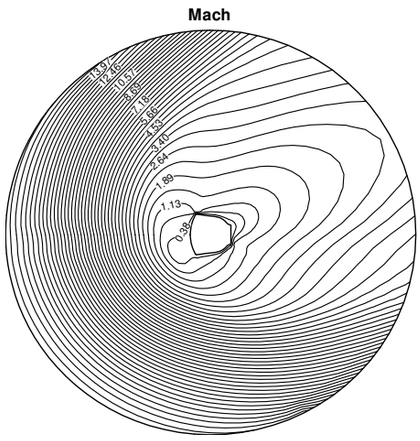

(a) Mach number contours with $\alpha = 30°$

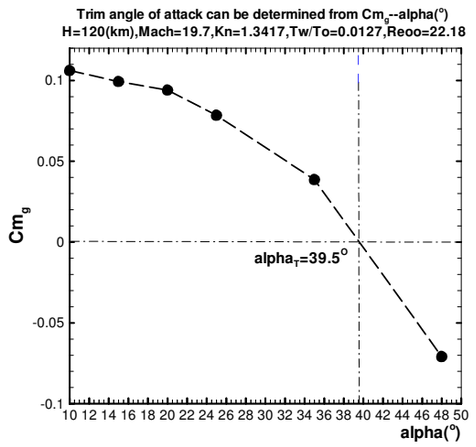

(b) Pitching moment coefficient C_{m_g} vs $\alpha(°)$

Fig. 38. Hypersonic rarefied flow past spacecraft shape for $Kn_\infty = 1.3417$, $M_\infty = 19.7$, $\mathrm{Re}_\infty = 22.18$.

To further study the flying flow problem of the spacecraft shape in high rarefied flow regime, the hypersonic flow state for the case of $Kn_\infty = 1.3417$, $M_\infty = 19.7$, $\mathrm{Re}_\infty = 22.18$ with the flight altitude of $H = 120km$ is computed. Fig.38(a) presents the Mach number contours in the symmetric plane past the body with the angle of attack of $\alpha = 30°$. It can be shown from Fig.38(a) that it exists a large disturbed region of flow with the strong compressing phenomena in front of the body, which is completely different from the near-continuum transitional flow depicted in Fig.37(a). Further more, the computed trim angle of attack can be obtained as $\alpha_{Cal} = 39.5°$ from Fig.38(b), where the pitching moment coefficient C_{mg} is plotted as a function of angle of attack α with $\alpha = 10°$, $15°$, $20°$, $25°$, $35°$, $48°$. The above computations are nicely consistent with the theoretical prediction and affirm the flow phenomena past the complex shape.

9. Concluding remarks

In this study, the gas-kinetic unified algorithm is studied and developed to solve the complex flow problems in perfect gas from rarefied transition to continuum flow regimes. The present numerical method uses the non-linear Boltzmann model equation describing microscopic molecular transport phenomena as the starting point for the computation, the single velocity distribution function equation is transformed into hyperbolic conservation equations with non-linear source terms by introducing the discrete velocity ordinate method of gas kinetic theory. Based on the decoupling technique on molecular movement and collision in the DSMC method, the time-splitting method for the unsteady equation is used to split up the discrete velocity distribution function equations into the colliding relaxation equations and the convective movement equations, and then the NND finite difference scheme is employed to solve the convective equations and the second-order Runge-Kutta method is used to numerically simulate the colliding relaxation equations. The gas-kinetic boundary conditions are studied and numerically implemented by directly acting on the velocity distribution function. The discrete velocity numerical quadrature techniques for different Mach number flows are developed and applied to evaluate the macroscopic flow moments over the velocity space. After constructing the present gas-kinetic numerical scheme, the multi-processing strategy and parallel implementation technique suitable for the gas-kinetic numerical method have been studied, and then the parallel processing software has been developed for solving three-dimensional complex flow problems. To test the feasibility of the present unified algorithm in solving the gas flows from rarefied transition to continuum regime, the one-dimensional shock-tube and shock-structure problems, the flows past two-dimensional circular cylinder, and the flows around three-dimensional sphere and spacecraft shape with various Knudsen numbers and different Mach numbers are simulated. The computational results are found in high resolution of the flow fields and good agreement with the relevant theoretical, DSMC, N-S and experimental results. It has been shown from the above computations that the results of the present method aren't sensitive to the grid spacing in the physical space or the velocity space if only the computing precision be satisfied, however, the finer is the grid, the better should be the precision of the results for certain at the expense of more computing memory and time. The present method is very stable and robust without the limitation of the cell size, unlike the DSMC method which exists statistical fluctuations and requires that the grid spacing have to be less than the mean free path, in general, the computational speed of the present method seems be faster than the DSMC method in computing one- and two-dimensional problems of the rarefied flows. However, the computer time required for the present method increases as the Knudsen number decreases. In the computation of the continuum flow, as the molecular mean collision time is generally smaller than the time step determined by the stable condition of the finite difference scheme, then the convergent speed of the present method seems be slower than that of the Navier-Stokes solver for the continuum flow regime, especially in the computations of three-dimensional continuum flows.

As the possible engineering applications involving atmosphere re-entry, the gas-kinetic numerical algorithm is employed to study the three-dimensional hypersonic flows and aerodynamic phenomena around sphere and spacecraft shape covering various flow regimes by parallel computing. It's shown by the study that the parallel algorithm has not only high parallel efficiency, but also good expansibility. The concurrent calculations show that the present parallel algorithm can effectively simulate the three-dimensional complex

flows from various flow regimes. The computed results match the relevant experimental data and DSMC results well, and the peculiar flow phenomena and mechanisms from various flow regimes are explored. It can be tasted from this study that the present gas-kinetic numerical algorithm directly solving the Boltzmann simplified velocity distribution function equation may provide an important and feasible way that complex hypersonic aerothermodynamic problems and flow mechanisms from rarefied flow to continuum regimes can be effectively studied with the aid of the power of parallel computer systems. As this work is only the beginning of the study of hypersonic flows by solving the Bolzmann-type velocity distribution function, farther investigations on the kinetic models for real-gas non-equilibrium effects involving internal energy and chemical reaction, and the efficiency and improvement of the present gas-kinetic numerical method, et al. need to be studied in more detail in the future

10. References

Abe, T. & Oguchi, H. 1977 A Hierarchy Kinetic Model and Its Applications. *Progress in Astronautics and Aeronautics*, Vol.51, edited by Potter J.I., AIAA, NewYork, 781-793.

Alsmeyer, H. 1976 Density Profiles in Argon and Nitrogen Shock Waves Measured by the Absorption of an Electron Beam, *J. Fluid. Mech*. 74 (3), 497.

Andries, P., Le Tallec, P., Perlat, J. & Perthame, B. 2000 The Gaussian-BGK model of Boltzmann equation with small Prandtl number, *European J. of Mechanics: B Fluids* 19 (6), 813.

Andries, P. & Perthame, B. 2000 The ES-BGK Model Equation with Correct Prandtl Number, in *Proc. of 22nd International Symposium on Rarefied Gas Dynamics*, Sydney, Australia, edited by T. J. Bartel and M. A. Gallis (AIP Conference Proceedings, Melville, New York, 2001), Vol.585, 30-36.

Aoki, K., Kanba, K. & Takata, S. 1997 Numerical Analysis of a Supersonic Rarefied Gas Flow past a Flat Plate. *Phys. Fluids* 9(4), 1144-1161.

Aristov V. V. 2001 *Direct Methods for Solving the Boltzmann Equation and Study of Nonequilibrium Flows*. Fluid Mechanics and its Applications, Vol.60, Kluwer Academic Publishers.

Bhatnagar, P. L., Gross, E. P. & Krook, M. 1954 A Model for Collision Processes in Gases. I. Small Amplitude Processes in Charged and Neutral One-Component Systems. *Phys. Rev*. 94, 511.

Bird, G. A. 1970 Aspects of the Structure of Strong Shock Waves. *Phys. Fluids* 13(5), 1172-1177.

Bird, G. A. 1994 *Molecular Gas Dynamics and the Direct Simulation of Gas Flows*. Clarendon Press, Oxford.

Boltzmann L. 1872 *Sber. Akad. Wiss Wien. Abt. II* 66, 275.

Brittin W. E. 1967 *Lectures in Theoretical Physics: Kinetic theory*, Volume IX C, Gordon and Breach, Science publishers, New York / London / Paris.

Celenligil, M. C., Moss, J. N. & Blanchard, R. C. 1991 Three-Dimensional Rarefied Flow Simulations for the Aeroassist Flight Experiment Vehicle. *AIAA Journal* 29(1), 52-57.

Cercignani, C. & Tironi G. 1967 Nonlinear heat transfer between two parallel plates at large temperature ratios. *Rarefied Gas Dynamics*, edited by Brundin C. L., Academic Press, New York, Vol.1, 441-453.

Cercignani, C. & Lampis M. 1971 Kinetic models for gas-surface interactions, Transport Theory and Stat. Phys., 1, 101-114.

Cercignani, C. 1984 *Kinetic Theories and the Boltzmann Equation*. Lecture Notes in Mathematics, Springer-Verlag, Berlin.

Cercignani C. 1994 The Mathematical Theory of Dilute Gases, Springer-Verlag, New York.

Cercignani, C. 2000 *Rarefied Gas Dynamics: from Basic Concepts to Actual Calculations*. Cambridge University Press, Cambridge.

Chapmann, S. & Cowling, T. G. 1970 *The Mathematical Theory of Non-Uniform Gases*. 3rd ed. Cambridge Univ. Press.

Chu, C. K. 1965 Kinetic-Theoretic Description of the Formation of a Shock Wave. *Physics of Fluids* 8(1), 12-22.

Dai, J. W., Yang, Y. G. & Li, X. G. 2004 Investigation of Rarefied Gas Aerodynamics of Spacecraft Shape in low density wind tunnel, *Tech. Rep. No. S423.15*, Hypersonic Aerodynamics Institute, China Aerodynamic Research and Development Centre.

Gilbarg, D. & Paolucci, D. 1953 The structure of shock waves in the continuum theory of fluids. *J. Rat. Mech. Anal*. 2, 617-642.

Grad 1949 On the kinetic theory of rarefied gases. *Commun. Pure Appl. Math.* 2, 331-407.

Golub, G. H. & Welsch, J. 1981 Calculation of Gauss Quadrature Rules, *Tech. Rep. No. CS81*, Computer Science Dept., Stanford University.

Henrici P. 1958 The Quotient-Difference Algorithm. *Nat. Bur. Standards Appl. Math. Series* 49, 23-46.

Holway Jr., L. H. 1963 Approximation Procedures for Kinetic Theory. Ph.D. Thesis, Harvard.

Holway Jr., L. H. 1966 New Statistical Models for Kinetic Theory, Methods of Construction. *Phys. Fluids* 9(9), 1658.

Huang, A. B. & Giddens, D. P. 1967 The Discrete Ordinate Method for the Linearized Boundary Value Problems in Kinetic Theory of Gases. *Proc. of 5th International Symposium on Rarefied Gas Dynamics*, edited by Brundin C. L., New York, Vol.1, 481-486.

Ivanov, M. S. & Gimelshein, S. F. 1998 Computational Hypersonic Rarefied Flows. *Annu. Rev. Fluid Mech.* 30, 469-505.

Kim C. & Jameson, A. 1998 A Robust and Accurate LED-BGK Solver on Unstructured Adaptive Meshes. *J. Comput. Phys*. 143(2), 598.

Kolobov, V.I., Arslanbekov, R.R., Aristov, V.V., Frolova, A.A. & Zabelok, S.A. 2007 Unified solver for rarefied and continuum flows with adaptive mesh and algorithm refinement. *J. Comput. Phys.* 223, 589-608.

Kogan, M. N. 1958 On the Equations of Motion of a Rarefied Gas. *Appl. Math. Mech.* 22, 597.

Kopal, Z. 1955 *Numerical Analysis*, Chapman & Hull Ltd., London

Koppenwallner, G. & Legge, H. 1985 Drag of Bodies in Rarefied Hypersonic Flow. *AIAA Paper 85-0998*, Progress in Astronautics and Aeronautics: Thermophysical Aspects of Re-entry Flows, Vol.103, edited by Moss J.N. & Scott C.D., New York, 44-59.

Kuščer I., Možina, Krizanic F. 1974 The Knudsen model of thermal accommodation. In Rarefied Gas Dynamics, edited by Dini et al., Vol.I, 97-108, Editrice Tecnico-Scientifica, Pisa.

Li, Z. H. & Xie, Y. R. 1996 Technique of Molecular Indexing Applied to the Direct Simulation Monte Carlo Method. *Proc. of 20th International Symposium on Rarefied Gas Dynamics*, edited by C. Shen, Beijing: Peking University Press, 205-209.

Li, Z.H. & Zhang, H.X. 2000 Study on Gas Kinetic Algorithm for Flows from Rarefied Transition to Continuum, *Proc. of 22nd International Symposium on Rarefied Gas Dynamics*, ed. by Bartel T.J. and Gallis M.A., Sydney, Australia, Jul. 9-14, Vol.585, 628-636.

Li, Z. H. 2001, *Study on the Unified Algorithm from Rarefied Flow to Continuum*, Ph. D. thesis, China Aerodynamics Researchment and Development Center.

Li, Z. H. & Zhang, H. X. 2003 Numerical Investigation from Rarefied Flow to Continuum by Solving the Boltzmann Model Equation. *Int. J. Numer. Meth. Fluids*, 42, 361-382.

Li, Z.H. 2003 Applications of gas kinetic unified algorithm for flows from rarefied transition to continuum, Post-doctor Dissertation, Beijing: Tsinghua University.

Li, Z. H. & Zhang, H. X. 2004a Study on Gas Kinetic Unified Algorithm for Flows from Rarefied Transition to Continuum. *J. Comput. Phys.*, 193(2), 708-738.

Li, Z. H. & Zhang, H. X. 2004b Gas kinetic algorithm using Boltzmann model equation, Computers and Fluids, 33, 967-991.

Li, Z. H. & Zhang, H. X. 2007 Gas-Kinetic Numerical Method Solving Mesoscopic Velocity Distribution Function Equation, *Acta Mechanica Sinica*, 23(3), 121-132.

Li, Z. H. & Zhang, H. X. 2008 Gas-kinetic description of shock wave structures by Boltzmann model equation, Inter. J. of Comput. Fluid Dyna., 22(9), 623-638.

Li, Z. H. & Zhang, H. X. 2009a Gas-kinetic numerical studies of three-dimensional complex flows on spacecraft re-entry. *J. Comput. Phys.*, 228(2), 1116-1138.

Li, Z. H. & Zhang, H. X. 2009b Study on the unified algorithm for three-dimensional complex problems covering various flow regimes using Boltzmann model equation, *Science in China (Series G)*, 52(1), 124-138.

Macrossan, M.N. & Oliver, R. I. 1993 A kinetic theory solution method for the Navier-Stokes equations. *Int. J. Numer. Meth. Fluids,* 17, 177.

Maslach, G. J. & Schaaf, S. A. 1963 Cylinder Drag in the Transition from Continuum to Free-Molecule Flow, *Phys. Fluids* 16(3), 315-321.

May, G., Srinivasan, B. & Jameson, A. 2007 An improved gas-kinetic BGK finite-volume method for three-dimensional transonic flow. *J. Comput. Phys.* 220, 856-878.

Mieussens, L. 2000 Discrete-velocity models and numerical schemes for the Boltzmann-BGK equation in plane and axisymmetric geometries. *J. Comput. Phys*. 162(2), 429-466.

Morinishi, K. & Oguchi H. 1984 A Computational Method and its Application to Analyses of Rarefied Gas Flows. *Proc. of 14th International Symposium on Rarefied Gas Dynamics*, Tsukubva, Japan, edited by H. Oguchi, Tokyo:University of Tokyo Press, 1, 149-158.

Moschetta, J.M. & Pullin D. 1997 A Robust Low Diffusive Kinetic Scheme for the Navier-Stokes/Euler Equations. *J. Comput. Phys*. 133, 193-204.

Muckenfuss, C. 1962 Some Aspects of Shock Structure According to the Bimodal Model, *Phys. Fluids* 5, 1325-1336.

Nocilla S. 1961 On the interaction between stream and body in free-molecule flow. In Rarefied Gas Dynamics, edited by L. Talbot, 169, Academic Press, New York.

Park, D. C. 1981 *The Kinetic Theory of Gases with Applications in Rarefied Gas Dynamics*. University of Strathclyde, Scotland.

Peter, P. W & Harry, A. 1962 Wind Tunnel Measurements of Sphere Drag at Supersonic Speeds and Low Reynolds. *J. of Fluid Mechanics* 10, 550-560.

Pham-Van-Diep, G.C., Erwin, D.A. & Muntz, E.P. 1991 Testing Continuum Descriptions of Low Mach Number Shock Structures, *J. Fluid Mech.*, 232, 403-413.

Prendergast, K. H. & Xu, K. 1993 Numerical hydrodynamics from gas-kinetic theory. *J. Comput. Phys*. 109, 53.

Reitz, R. D. 1981 One-Dimensional Compressible Gas Dynamics Calculations Using the Boltzmann Equation. *J. Comput. Phys*. 42, 108-123.

Riedi, P. C. 1976 *Thermal physics: An Introduction to Thermodynamics, Statistical Mechanics and Kinetic Theory*. The Macmillan Press Ltd., London.

Roger, F. & Schneider J. 1994 Deterministic Method for Solving the Boltzmann Equation. *Rarefied Gas Dynamics: Theory and Simulations*, edited by Shizgal B. & Weaver D. P., AIAA, Vol.159, 335-343.

Segal, B. M. & Ferziger, J. H. 1972 Shock-Waves Structure Using Nonlinear Model Boltzmann Equations. *Phys. Fluids* 15, 1233.

Shakhov, E. M. 1968 Generalization of the Krook Kinetic Relaxation Equation. *Fluid Dynamics* 3(1), 95.

Shakhov, E. M. 1984 Kinetic Model Equations and Numerical Results. *Proc. of 14th International Symposium on Rarefied Gas Dynamics*, edited by Oguchi H., Tokyo: University of Tokyo Press, Vol.1, 137-148.

Sharipov F. 2003 Hypersonic Flow of Rarefied Gas Near the Brazilian Satellite During its Re-entry into Atmosphere. *Brazilian Journal of Physics* 33(2), 398-405.

Shizgal, B. 1981 A Gaussian Quadrature Procedure for Use in the Solution of the Boltzmann Equation and Related Problems. *J. Comput. Phys*. 41, 309-328.

Tan Z. & Varghese P. 1994 The Δ-ε Method for the Boltzmann Equation. *Journal of Computational Physics* 110, 327-340.

Tcheremissine F. G. 1989 Advancement of the Method of Direct Numerical Solving of the Boltzmann Equation. *Rarefied Gas Dynamics: Theoretical and Computational Techniques*, edited by Muntz E. P. & Campbell D. H., AIAA, Vol.118, 343-358.

Titarev V. A. & Shakhov E. M. 2002 Heat Transfer and Evaporation from a Plane Surface into a Half-Space upon a Sudden Increase in Body Temperature. *Fluid Dynamics* 37(1), 126-137.

Tsien, H. S. 1946 Superaerodynamics, Mechanics of Rarefied Gases. *J. Aeronautical Science* 13(12), 653-664.

Vincenti, W. G. & Kruger, C. H. 1965 *Introduction to Physical Gas Dynamics*. Wiley, New York.

Vogenitz, F. W., Bird, G. A., Broadwell, J. E. & Rungaldier H. 1968 Theoretical and Experimental Study of Rarefied Supersonic Flows about Several Simple Shapes. *AIAA Journal* 6(12), 2388-2394.

Welander, P. 1954 On the Temperature Jump in a Rarefied Gas. *Ark. Fys.* 7, 507.

Xu, K. 1998 *Gas-Kinetic Schemes for Unsteady Compressible Flow Simulations*, 29th CFd Lecture Series 1998-03, Von Karman Institute for Fluid Dynamics, Lecture Series, Belgium, Feb.23-27.

Xu, K., Mao, M. & Tang, L. 2005 A multidimensional gas-kinetic BGK schemes for hypersonic viscous flow. *J. Comput. Phys.* 203, 405-421.

Xu K. 2001 A Gas-kinetic BGK Schemes for the Navier-Stokes Equations and Its Connection with Artificial Dissipation and Godunov Method. *J. Comput. Phys*. 171, 289-335.

Xu, K. & Li, Z. H. 2004 Microchannel flow in the slip regime: gas-kinetic BGK-Burnett solutions. *J. Fluid Mech*. 513, 87-110.

Yang, J.Y. & Hsu, C.A. 1992 High Resolution, Nonoscillatory Schemes for Unsteady Compressible Flows, *AIAA J*. 30, 1570-1575.

Yang, J. Y. & Huang, J. C. 1995a Rarefied Flow Computations Using Nonlinear Model Boltzmann Equations. *J. Comput. Phys*. 120, 323-339.

Yang, J. Y. & Huang, J. C. 1995b Numerical solution of the nonlinear model Boltzmann Equation. Proc. R. Soc. Lond. A 448, 55-77.

Zhang, H. X. & Zhuang F. G. 1992 NND Schemes and Their Application to Numerical Simulation of Two- and Three-Dimensional Flows. *Advances in Applied Mechanics* 29, 193.

Любимов, А. Н. and Русањов В. В. 1970, ТЕЧЕНИЯ ГАЗА ОКОЛО ТУПЫХ ТЕЛ, Частъ II, *ИЗДАТЕЛЬСТВ «НАУКА»* , p.32-33, МОСКВА, (1970).

Advances in Spacecraft Technologies

Edited by Dr Jason Hall

ISBN 978-953-307-551-8
Hard cover, 596 pages
Publisher InTech
Published online 14, February, 2011
Published in print edition February, 2011

The development and launch of the first artificial satellite Sputnik more than five decades ago propelled both the scientific and engineering communities to new heights as they worked together to develop novel solutions to the challenges of spacecraft system design. This symbiotic relationship has brought significant technological advances that have enabled the design of systems that can withstand the rigors of space while providing valuable space-based services. With its 26 chapters divided into three sections, this book brings together critical contributions from renowned international researchers to provide an outstanding survey of recent advances in spacecraft technologies. The first section includes nine chapters that focus on innovative hardware technologies while the next section is comprised of seven chapters that center on cutting-edge state estimation techniques. The final section contains eleven chapters that present a series of novel control methods for spacecraft orbit and attitude control.

How to reference

In order to correctly reference this scholarly work, feel free to copy and paste the following:

Zhi-Hui Li (2011). Gas-Kinetic Unified Algorithm for Re-Entering Complex Problems Covering Various Flow Regimes by Solving Boltzmann Model Equation, Advances in Spacecraft Technologies, Dr Jason Hall (Ed.), ISBN: 978-953-307-551-8, InTech, Available from: http://www.intechopen.com/books/advances-in-spacecraft-technologies/gas-kinetic-unified-algorithm-for-re-entering-complex-problems-covering-various-flow-regimes-by-solv

INTECH
open science | open minds

InTech Europe
University Campus STeP Ri
Slavka Krautzeka 83/A
51000 Rijeka, Croatia
Phone: +385 (51) 770 447
Fax: +385 (51) 686 166
www.intechopen.com

InTech China
Unit 405, Office Block, Hotel Equatorial Shanghai
No.65, Yan An Road (West), Shanghai, 200040, China
中国上海市延安西路65号上海国际贵都大饭店办公楼405单元
Phone: +86-21-62489820
Fax: +86-21-62489821

IntechOpen